NASA CONTRACTOR REPORT

NASA CR-1312

c. 1

NASA CR-1312

THEORETICAL INVESTIGATIONS OF R-F INDUCTION HEATED PLASMAS

by Arthur E. Mensing and Laurence R. Boedeker

Prepared by
UNITED AIRCRAFT CORPORATION
East Hartford, Conn.
for

NATIONAL AERONAUTICS AND SPACE ADMINISTRATION • WASHINGTON, D. C. • APRIL 1969

NASA CR-1312

THEORETICAL INVESTIGATIONS

OF R-F INDUCTION HEATED PLASMAS
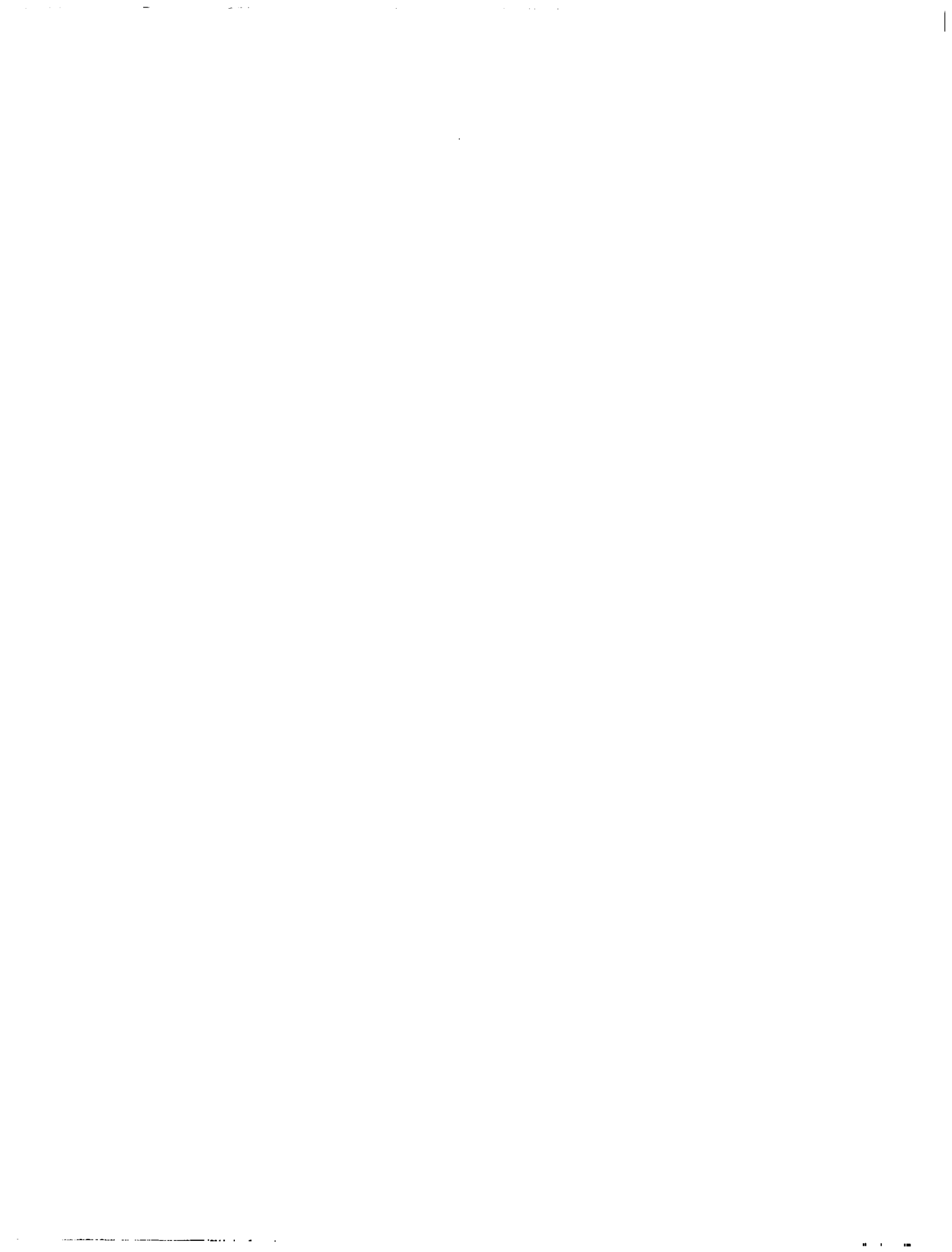
By Arthur E. Mensing and Laurence R. Boedeker

Distribution of this report is provided in the interest of information exchange. Responsibility for the contents resides in the author or organization that prepared it.

Issued by Originator as Report No. G-910091-18

Prepared under Contract No. NASw-847 by
UNITED AIRCRAFT CORPORATION
East Hartford, Conn.

for

NATIONAL AERONAUTICS AND SPACE ADMINISTRATION

<u>Theoretical Investigations of R-F Induction Heated Plasmas</u>

TABLE OF CONTENTS

TABLE OF CONTENTS (Continued)

Theoretical Investigations of R-F Induction Heated Plasmas

SUMMARY

Theoretical analyses were made to investigate the power deposition and energy
removal in radio-frequency induction heated plasmas. These investigations were
directed toward the high-power, high-pressure, radiating r-f plasmas that are being
used to simulate the thermal environment of the nuclear light bulb reactor·

Two related investigations are described in this report. In one, the power
deposition and energy dissipation characteristics of infinite-cylinder r-f heated
argon plasmas at pressures of 1.0 and 10 atm were studied. It was assumed that the
thermal and electrical conductivities varied with temperature, that the gas radiation
per unit volume varied with both temperature and pressure, and that the plasma was
optically thin. The electromagnetic field equations, energy equation, and heat con-
duction equation were integrated numerically starting with specified values of tem-
perature and axial magnetic field at the centerline. Generalized curves suitable
for design and analysis of experiments were constructed. These curves show the
relationships between the radius of the plasma, the axial magnetic field external
to the plasma, the power radiated, and the radiation efficiency (the power radiated
divided by the sum of the power radiated and the power conducted away from the
plasma). The results also show the importance of gas radiation on the character-
istics of the plasmas.

In the second investigation, the coupling between the plasma discharge and the
r-f generator was studied using an infinite-cylinder, constant-conductivity model.
Analyses performed by other investigators were combined and extended to develop an
analysis more useful in the nuclear light bulb reactor simulation program. The
analysis was used to investigate the effects of discharge power, reactive power,
and discharge size on the surface radiation heat flux and to examine the effect of
r-f frequency shifts on matching. In addition, an expression was derived from which
the magnetic pressure at the center of an r-f discharge can be calculated.

RESULTS AND CONCLUSIONS

1.   In analyses of power deposition and energy removal in r-f induction heated plasmas, it is important to include plasma radiation as an energy loss mechanism at plasma pressures of about 1.0 atm and above. For example, for a 1.0-atm argon plasma with a centerline temperature of 10,000 deg K and a centerline axial magnetic field of 5.0 amp-turns/cm, the calculated power deposition per unit length of the plasma is 0.153 kw/cm when radiation is neglected; the calculated power deposition is 3.27 kw/cm when radiation is included, even though the power radiated is only 1.14 kw/cm. This large difference in power deposition is due to grossly different radial distributions of temperature which cause large differences in the thermal and electrical conductivities.

2.   In r-f induction heated plasmas, radiation causes the peak temperature to occur in an annulus around the centerline rather than on the centerline as in d-c plasmas.

3.   The analysis developed in this report may be used to construct generalized plots describing r-f plasmas. If the type of gas, the pressure and the r-f frequency are specified, then the following four parameters of interest for simulation of the nuclear light bulb reactor can be used to form these plots: (1) the power radiated, (2) the radius of the plasma, (3) the energy loss by conduction, and (4) the axial magnetic field external to the plasma. If the radius of the plasma is determined by fluid dynamics considerations, then specification of any one of the three remaining parameters determines the other two.

4.   For a uniform electrical conductivity discharge, the transfer of power from the magnetic field to the discharge can be characterized by a dimensionless coupling coefficient defined as the ratio of the total discharge power to the reactive power in the r-f induction coil. (The reactive power is approximately one-half the product of coil voltage and coil current; the maximum voltage and current determine the limits of resonator performance.) When the radius of the discharge approaches the radius of the coil, the coupling coefficient approaches unity. When the radius of the discharge becomes small compared with the radius of the coil, significant increases in reactive power are required for a given discharge power.

5.   An increase in either the discharge-diameter-to-skin-depth ratio or the discharge-to-coil radius ratio increases the effective coil resistance and decreases the effective coil inductance. For discharge-to-coil radius ratios less than about 0.35, frequency shifts (from the unloaded resonant frequency) of less than about ten times the unloaded resonator bandwidth are required to provide proper impedance matching, i.e., reactance equal to zero. These frequency shifts are usually less than 2 percent of the resonant frequency.

2

6.   Neglecting momentum changes that might occur in the plasma, time-averaged magnetic pressure gradients in an r-f plasma cause an increase in pressure at the center of the plasma. This pressure increase has a limiting value of $B_O^2/4\mu_O$, where B_O is the peak magnetic field strength outside the discharge and μ_O is the magnetic permeability. For a 1.0-cm-dia inductively heated plasma having a discharge-diameter-to-skin-depth ratio of 3.5 within an 8-cm-dia coil, the pressure increase at the plasma centerline was 0.018 atm when 600 kw of power were deposited in the plasma.

INTRODUCTION

An experimental and theoretical investigation of gaseous nuclear rocket technology is being conducted by United Aircraft Research Laboratories under Contract NASw-847 administered by the joint AEC-NASA Space Nuclear Propulsion Office. The research performed under this contract is primarily applicable to the vortex-stabilized nuclear light bulb rocket concept described in Ref. 1. In this concept, hydrogen propellant seeded with a small amount of tungsten is heated by thermal radiation passing through an internally cooled transparent wall located between the gaseous uranium fuel and the propellant. A buffer gas is injected tangent to the inner surface of the transparent wall to establish a vortex flow which is utilized to isolate the gaseous nuclear fuel from the transparent wall.

Non-nuclear laboratory simulation of the flow and radiant heat transfer characteristics of a nuclear light bulb engine can be accomplished using an electrical discharge to add energy to the central simulated-fuel region of the vortex. A high-power radio-frequency induction heater has been selected for this purpose. Using the UARL 1.2-megw r-f induction heater, efforts are being made to increase the power deposited in the discharge and, through use of high pressures and seed materials, to increase the power radiated from the discharge. The current status of this work is discussed in Ref. 2.

R-F induction heaters have been used for many years to create and heat plasmas. However, certain of the phenomena involved which are of importance to the nuclear light bulb research program are not fully understood. Accordingly, it is the purpose of the present study to theoretically describe and investigate three aspects of plasma induction heating: (1) the power addition and energy dissipation occurring in the plasma, (2) the coupling coefficient and reflected impedance of a constant-conductivity plasma, and (3) the magnetic pressure created by the interaction of the r-f field and the plasma.

Equipment for adding energy to a plasma by r-f induction heating usually has three main components: the power supply; the r-f power amplifier; and the resonator, which consists of a capacitor section and an induction coil surrounding the plasma. There is often strong interaction between the characteristics of the power amplifier and the resonator. In general, the performance of a resonator in adding power to a plasma is dependent upon the characteristics of the power amplifier. However, in the present report, only the interaction between the resonator (or the electromagnetic fields it produces) and the plasma is considered. Additional analyses are required to solve the complete interaction problem among the various components.

COMBINED ELECTROMAGNETIC AND THERMAL ANALYSIS OF R-F GAS DISCHARGES

Background of Problem

It has been shown experimentally that high-power and high-power-density plasmas can be created by means of radio-frequency induction heating (Refs. 2 and 3). However, a sufficiently general theoretical analysis to determine the induced electromagnetic fields, conduction and radiation heat fluxes, and temperatures within the plasma has not been developed. A comprehensive analysis of the phenomena of r-f plasma heating is desirable for guiding experiments described in Ref. 2 and for obtaining a better understanding of the heating process. Because of the large variation with temperature of the electrical conductivity of a plasma, the classical solutions for induction heating of constant-electrical-conductivity metal work pieces (e.g., Ref. 4) are not applicable for determining the details of plasma heating although, as shown in a later section of this report, a constant equivalent electrical conductivity can be used to describe the coupling between the r-f generator and the plasma.

In the present analysis, the relationship between temperature and electrical conductivity must be known to enable the temperature distribution within the plasma to be calculated. Since the temperature is dependent upon the heat flux within the plasma, the heat transfer equations must be coupled with the electromagnetic equations which describe the power deposition. In Refs. 5 and 6, the conduction heat flux equation was solved simultaneously with the electromagnetic field equations and closed-form solutions were obtained. However, energy lost by radiation from the plasma was neglected. In addition, the electrical conductivity was assumed to be constant in Ref. 6 and to be a simple function of radius in Ref. 5. The desire to obtain closed-form analytic solutions did, of course, require the simplifying assumptions employed in Refs. 5 and 6. These assumptions limit the applicability of the solutions.

In the Soviet work described in Refs. 7 and 8, the one-dimensional differential equations for the heat flux and the electromagnetic fields were integrated numerically. The variations of gas radiation, electrical conductivity, and thermal conductivity with temperature were prescribed. This method appears to adequately describe the r-f induction heating of a plasma. However, only a relatively few results were presented in Refs. 7 and 8 and, since the results were obtained by numerical integration, extrapolation to conditions other than those presented is not possible. In addition, the variations of electrical conductivity, thermal conductivity and gas radiation with temperature that were used in Refs. 7 and 8 are not widely used by investigators in the U. S.

The objectives of this portion of the study was to establish a computer program for numerically integrating the heat flux and electromagnetic equations and to obtain solutions over extended ranges of operating conditions. The variations of gas properties with temperature for this computer program were derived from the best available data and theoretical predictions.

Method of Analysis

The model used in the following one-dimensional analysis (i.e., variation in the radial direction only) consists of an axisymmetric cylindrical plasma, infinite in axial extent. A sketch of the model employed is shown in Fig. 1. The plasma radius is r_6 and is defined as the radius at which the temperature is 1000 deg K.* All gas properties within the plasma are dependent upon temperature. The plasma is assumed to be optically thin (no self-absorption), in local thermodynamic equilibrium, and purely resistive. Power is added to the plasma by the flow of induced currents and is removed by both radiation and thermal conduction. It is assumed that there are no convection losses within the plasma.

For an annulus of thickness dr within the plasma at radius r, the sum of (1) the energy per unit length per unit time conducted into the annulus at radius r plus (2) the energy per unit length per unit time added to the annulus by circulating induced currents is equal to the sum of (3) the energy per unit length per unit time conducted out of the annulus at radius r + dr plus (4) the energy per unit length per unit time radiated from the annulus. Using the notation shown in Fig. 1, this equality may be written as

$$\overline{W}_C + (2\pi r\,dr)\,\sigma\,E_\theta^{\;2} = \overline{W}_C + \left(\frac{d\overline{W}_C}{dr}\,dr\right) + (2\pi r\,dr)\,\overline{W}_{V_{RAD}} \qquad (1)$$

or

$$\frac{d\overline{W}_C}{dr} = 2\pi r\left(\sigma\,E_\theta^{\;2} - \overline{W}_{V_{RAD}}\right) \qquad (2)$$

---

* The symbol r_6 is used to be consistent with nomenclature used in Ref. 2 for the plasma radius.

Fourier's law of heat conduction for the plasma annulus is

$$\frac{dT}{dr} = -\frac{\overline{W}_c}{2\pi r \lambda} \tag{3}$$

Maxwell's equations for a conductor having a permeability of 1.0 with negligible displacement currents are, in vector form,

$$\nabla \times \vec{E} = -\mu_0 \frac{\partial \vec{H}}{\partial t} \tag{4a}$$

and

$$\nabla \times \vec{H} = \sigma \vec{E} \tag{4b}$$

For the one-dimensional problem (i.e., variations with radius only) Eqs. (4a) and (4b) can be written as

$$\frac{1}{r}\frac{\partial}{\partial r}(r E_\theta) = -\mu_0 \frac{\partial H_z}{\partial t} \tag{5a}$$

and

$$\frac{\partial H_z}{\partial r} = \sigma E_\theta \tag{5b}$$

For alternating fields, the electric and magnetic fields are

$$E_\theta = E_{\theta_P} e^{i(\omega t - \phi_E)} \tag{6a}$$

$$H_z = H_{z_P} e^{i(\omega t - \phi_H)} \tag{6b}$$

where E_{θ_P} and H_{z_P} are the peak values of the electric and magnetic fields, respectively, and ϕ_E and ϕ_H are the respective field phase angles.

Substituting Eqs. (6) into Eqs. (5), preforming the indicated differentiation, and equating the real and imaginary parts,

$$\frac{dE_{\theta_P}}{dr} = -\frac{E_{\theta_P}}{r} - \mu_0 \omega H_{z_P} \sin(\phi_H - \phi_E) \tag{7a}$$

$$\frac{dH_{z_P}}{dr} = \sigma E_{\theta_P} \cos(\phi_H - \phi_E) \tag{7b}$$

and

$$\frac{d\phi_E}{dr} = \frac{\mu_0 \omega H_{z_P}}{E_{\theta_P}} \cos(\phi_H - \phi_E) \tag{8a}$$

$$\frac{d\phi_H}{dr} = -\frac{\sigma E_{\theta_P}}{H_{z_P}} \sin(\phi_H - \phi_E) \tag{8b}$$

Equations (8), (7), (3), and (2) provide a set of six first-order differential equations which must be solved simultaneously to determine the temperature, heat flux, and electric and magnetic fields within the plasma. To solve these equations it is first necessary to describe the variations of λ, σ, and $\overline{W}_{V_{RAD}}$ with temperature. All calculations performed in this study were made for argon. The gas properties of an argon plasma are fairly well documented at elevated temperatures throughout a wide range of pressures. In addition, most experiments involving r-f plasmas have employed argon as the working fluid.

Figure 2 presents the variation with temperature of the thermal conductivity, λ, of argon at 1.0 atm as presented in several references (Refs. 9 through 13). The solid line of Fig. 2 is the assumed variation of thermal conductivity that was used in all calculations in this study. This curve closely follows the calculated values of Ref. 13 which appear to agree best with experimentally measured values (Ref. 9). No variation of the thermal conductivity with pressure was included since

very little reliable data on this effect are available. The effect of pressure is believed to be small for the range of pressures considered in this study (1.0 to 10 atm); however, at higher pressures and temperatures, neglecting the pressure effect on thermal conductivity could cause erroneous results.

The variation of the electrical conductivity, σ, of argon with temperature is presented in Fig. 3. Curves from several sources (Refs. 13 through 16) are shown and the variation that was assumed in this study is indicated by the solid line. The variation assumed herein favored that of Ref. 14 since it is the most recent and probably the most accurate information available. Results from Ref. 14 show small differences in electrical conductivity with pressure (i.e., compare curves for 1.0 atm and 10 atm in Fig. 3). However, the scatter and uncertainty of the existing electrical conductivity information is greater than effects due to pressure; hence, for the purpose of this study, it was assumed that there is no variation of electrical conductivity with pressure. When more reliable data on the effects of pressure on thermal and electrical conductivities become available, they can be incorporated into the computer program.

The power per unit volume radiated from the plasma, $\overline{W}_{V_{RAD}}$, was determined as functions of both temperature and pressure by the method described in Appendix I. From a calculated equilibrium composition of argon (Fig. 4 and Ref. 17), the radiation from 71 argon lines and the continuum was calculated. The total radiation, $\overline{W}_{V_{RAD}}$ (i.e., the sum of the line and continuum), is presented in Fig. 5 versus temperature for pressures of 1.0 and 10 atm. The values of $\overline{W}_{V_{RAD}}$ used in Eq. (2) were obtained from the curves of Fig. 5. Included on Fig. 5 is a data point from the r-f experiments described in Ref. 18. The data were obtained at a pressure of 1.0 atm. The agreement between the theory described in Appendix I and the data of Ref. 18 is quite good. Both the theory and the data considered radiation only within the region of 3500 to 8500 Å.

From the assumed temperature variation of λ, σ, and $\overline{W}_{V_{RAD}}$, the set of equations (i.e., Eqs. (8a), (8b), (7a), (7b), (3), and (2)) can be solved once the appropriate boundary conditions are prescribed. At $r = 0$, $\overline{W}_c = 0$, $E_{\theta P} = 0$, and $\phi_H - \phi_E = \pi/2$. Since only the difference between ϕ_H and ϕ_E appears in the equations, the boundary conditions employed were at $r = 0$, $\phi_H = 0$, and $\phi_E = \pi/2$. The two remaining boundary conditions (on T and H_{z_P}) were also specified at the centerline. Physically, it would be more logical to specify the temperature at the edge of the plasma and the magnetic field external to the plasma. However, this results in mixed boundary conditions (i.e., some at $r = 0$ and some at $r = r_6$) and requires a complicated iteration technique. Thus, to simplify the calculating procedure, both temperature and magnetic field were specified at the centerline. The radius of the plasma, r_6, was determined, as previously stated, as that radius at which the temperature reaches 1000 deg K. Thus, the six boundary conditions were specified at the centerline (i.e., at $r = 0$ it was specified that $\overline{W}_c = 0$, $E_{\theta P} = 0$, $\phi_H = 0$, $\phi_E = \pi/2$, $T = T_{CL}$,

9

$H_{z_P} = H_{z_{CL}}$) and the six first-order differential equations (Eqs. (8a), (8b), (7a), (7b), (3), and (2)) were solved simultaneously by a straight-forward numerical integration technique beginning at the centerline and proceeding radially outward. The numerical integration technique employed was the third-order Runge-Kutta method described in most advanced calculus text books. The equations were programmed in dimensional form for the UNIVAC 1108 digital computer.

To check the accuracy of the numerical integration, a case was calculated in which the electrical conductivity was assumed constant (independent of temperature), and both the thermal conductivity and the power radiated were set equal to zero. For this case exact solutions for the field strengths can be calculated (see, for instance, Ref. 4 and following sections). In Fig. 6, the radial variation of the magnetic field as calculated by the numerical integration method is compared with the exact solution. The significance of the parameters κ and d/δ is discussed subsequently. The agreement shown in Fig. 6 is excellent.

Discussion of Results

Calculations were performed in which the centerline temperature, centerline axial magnetic field, and discharge pressure were varied. The results of one typical case are shown by the solid lines in Fig. 7. For this case the centerline temperature was 10,000 deg K, the centerline magnetic field was 5 amp-turns/cm, the pressure was 1.0 atm and the r-f frequency was 10 mHz. The variations of gas properties with temperature shown in Figs. 2, 3, and 5 were used. Figure 7 presents the radial variations of conduction heat flux, temperature, circumferential electric field, axial magnetic field, and magnetic and electrical field phase angles. As discussed in the previous subsection, the calculations begin with an assumed center-line temperature and axial magnetic field and procede in a radial direction until the temperature is less than 1000 deg K. At larger radii, the axial magnetic field is essentially constant; there is no heat addition, negligible radiation, and essentially constant thermal conductivity.

Of primary interest in Fig. 7 is the radial variation of temperature. The temperature peaks off the centerline at a radius within the plasma rather than at the centerline as is the case with d-c arcs. The peak is, of course, associated with the skin depth of the plasma such that power added to the plasma decreases substantially in the interior regions of the plasma. The off-axis peaking of the plasma temperature may be an important consideration in the design of a high-efficiency light source. The dashed curves shown in Fig. 7 were obtained by setting the gas radiation, $\overline{W}_{V_{RAD}}$, equal to zero. The same centerline conditions were used. It is evident that gas radiation is an important feature of the solution. Note that with no radiation, the temperature has a maximum value at the centerline. With radiation,

the maximum temperature occurs at a radius well away from the centerline. Thus, radiation is one factor which causes the off-axis peaking of temperature that has been experimentally observed in r-f plasmas (Refs. 2, 18, and 19). In experiments employing vortex discharges, high convective velocities near the centerline of the vortex could also contribute to this off-axis peaking.

Figure 7 also indicates an important result regarding the effect of radiation on the total required power deposition. For the example given in Fig. 7 (a center-line temperature of 10,000 deg K and a centerline axial magnetic field of 5 amp-turns/cm), the calculated power deposition per unit length of the plasma was 0.153 kw/cm when radiation was neglected; the calculated power deposition was 3.27 kw/cm when radiation was included, even though the power radiated was only 1.14 kw/cm. This large difference in power deposition is due to the grossly different radial distributions of temperature which cause large differences in the thermal and electrical conductivities. Thus, in analyses of power deposition and energy dissipation in r-f induction heated plasmas, it is important to include plasma radiation as an energy loss mechanism at plasma pressures of about 1.0 atm and above.

The temperature and axial magnetic field on the centerline are not too meaningful since they are really dependent parameters and cannot be independently chosen in any real plasma. Therefore, several cases were calculated with ranges of centerline temperatures and axial magnetic fields. The results of these calculations were then plotted using the axial magnetic field external to the plasma and the radius of the plasma as independent variables, and the power conducted out of the plasma and the power radiated as dependent variables. Figures 8 and 9 present these variations for pressures of 1.0 and 10 atm, respectively. The gas is argon and the r-f frequency is 10 mHz. Also shown in Figs. 8 and 9 are curves of constant radiated power per unit length, $\overline{W}_{RAD}$. These results are for a plasma which is assumed infinite in axial length. Since the plasma is infinite in length, the surrounding coil must also be infinite. For an infinite coil, the axial magnetic field external to a plasma is related to the coil current by

$$H_0 = \frac{N}{\ell_c} I_c \qquad (9)$$

where N/ℓ_c is the number of coil turns per unit length and I_c is the peak value of the coil current.

The results presented in Figs. 8 and 9 show that the size of the plasma and the magnetic field determine the power conducted and the power radiated from the plasma. At the edge of the plasma (i.e., $r = r_6$), a heat sink must exist to remove the power conducted from the plasma, $\overline{W}_{c_6}$ (see Fig. 1). To provide this heat sink at $r = r_6$,

it is required to have either a flow in which there are very large axial convective velocities or a cooled wall. Large convective flows at $r = r_6$ are desirable so that the plasma can be confined away from the chamber walls. Since it is also assumed that no convection exists within the plasma, small convective flows are required at radii less than r_6. Such a flow can be obtained using a confined vortex flow. It has been shown experimentally in Ref. 20 that a radial-inflow vortex has a radial stagnation streamline outside of which large axial flows exist while at radii less than the stagnation streamline a cell flow exists having small convective flows. Reference 20 also demonstrates that the radial position of the radial stagnation streamline can be controlled by adjusting the percentage of injected flow that is removed from the center of the vortex. Thus, a radial-inflow vortex has the desired combined characteristics of low convective flow within the plasma while providing a high convective flow which can act as a heat sink external to the plasma.

If the required radiated power and the size of the discharge are specified, then the required axial magnetic field and the power conducted to the heat sink outside the plasma (i.e., the large convective flow region) can be obtained from Figs. 8 and 9. In general, if the radius of the plasma is specified, then specification of any one of the three parameters H_o, $\overline{W}_{c_6}$, or $\overline{W}_{RAD}$ determines the other two. Use of curves of this type is of particular interest in the nuclear light bulb program where a high radiant heat flux per unit surface area of the discharge is being sought (Ref. 2).

In Figs. 10 and 11, the results shown in Figs. 8 and 9 are replotted so that the ordinate is the total power deposited in the plasma (i.e., the sum of the power conducted out of the plasma and the power radiated). Again, the abscissa is the axial magnetic field external to the plasma. Curves of constant plasma radius are shown. In addition, two other sets of lines are presented. One of these is the radiation efficiency, η_R, defined as

$$\eta_R = \frac{\overline{W}_{RAD}}{\overline{W}_{c_6} + \overline{W}_{RAD}} = \frac{\overline{W}_{RAD}}{\overline{W}_D / \ell} \tag{10}$$

The other set of curves, labeled κ_{eq}, is the equivalent coupling parameter that would exist if the total power, $\overline{W}_D / \ell$, were to be deposited in a cylinder of constant electrical conductivity having a radius r_6. The definition of κ for a constant conductivity plasma is

$$\kappa = \frac{1}{\sqrt{2}} \frac{2r_6}{\delta} \tag{11}$$

where δ is the skin depth. The variation of skin depth with conductivity and frequency is shown in Fig. 12. It is shown in the succeeding section that the power per unit length deposited in a plasma of constant electrical conductivity is

$$\frac{\overline{W}_D}{\ell} = \frac{1}{2}(2\pi f)\mu_0\left(H_0\right)^2\left(\pi r_6^2\right)Q \tag{12}$$

where Q is a magnetic flux integral. The variation of Q with κ is shown in Fig. 13. By equating $\overline{W}_D/\ell$ to $\overline{W}_{c6} + \overline{W}_{RAD}$ for a plasma of a given radius, r_6, with a given magnetic field external to the plasma, H_0, the value of Q can be determined and the resulting value of κ_{eq} can be found from Fig. 13. In Figs. 10 and 11 the cross-hatched regions are where the value of the calculated Q is greater than 0.37, the maximum value for a constant-conductivity cylinder; hence, κ_{eq} cannot be defined in these regions. Within the cross-hatched regions the plasma will absorb more power than an equivalent constant-conductivity cylinder of the same radius and same axial magnetic field. As a general rule, plasmas with low values of the equivalent coupling parameter have corresponding low values of radiation efficiency.

The data point shown on Fig. 10 has been obtained from the experiments of Ref. 18. In these experiments, approximately 900 w/cm of power was deposited into a 1.0-atm argon plasma. The plasma radius was determined from photographs to be 2.5 cm. From Fig. 10, the required axial magnetic field would be 27 amp-turns/cm and the radiation efficiency would be about 18 percent. The experiments of Ref. 18 gave a coil current of 75 amps for a coil having 0.4 turns/cm. Thus, the axial magnetic field in the experiments is calculated from Eq. (9) to be 30 amp-turns/cm, in very good agreement with values obtained from Fig. 10. The radiation efficiency for the experiments in Ref. 18 was measured to be about 10 percent, significantly lower than the value obtained from Fig. 10. Considering that the frequency of the experiments of Ref. 18 was 7.25 mHz compared with 10 mHz for the calculated curves of Fig. 10, and that three-dimensional effects were present in the experiments, the agreement between theory and experiment is quite good.

Several authors (Refs. 21 and 6) have reported that the diameter of an r-f induction heated plasma observed in experiments is approximately 3.5 times the skin depth (i.e., $\kappa = 2.5$). Since this phenomenon is not predicted by the calculated results shown in Figs. 8 through 11 nor in the results of Ref. 8, it may be that the experimentally observed plasma diameter-to-skin-depth ratio of 3.5 was caused by the interaction between the particular resonator and r-f power amplifier equipment used in those experiments. As discussed in the INTRODUCTION, this interaction has not been included in the present study.

It is interesting to note that for a given magnetic field and given plasma radius, two plasmas having different temperatures and heat fluxes can be obtained (Figs. 8 through 11). For the lower value of power deposition, the plasma absorbs very little power from the field and is a poor conductor. Conversely, for the higher power deposition, the radius of the plasma is greater than the skin depth, and thus the plasma is a good conductor. Experimental observations by many authors (e.g., Refs. 2, 3, and 21) tend to show that only those plasmas having the higher values of power deposition can be created. It appears that the lower-power plasmas are not produced experimentally and may not represent a physically real situation.

It should be noted that, in the high-heat-flux regions of Figs. 8 through 11, a substantial amount of uncertainty exists due to inaccuracies in the plasma properties (i.e., the electrical and thermal conductivities and the power radiated). In these high-heat-flux plasmas ($\overline{W}_D/\ell$ greater than approximately 10 kw/cm) the peak plasma temperatures exceed 20,000 deg K. The existing plasma properties are not accurate at these temperatures, and the assumption of an optically thin plasma may not be valid. Self-absorption will have a significant effect on these plasmas. It is planned to extend this analysis to include the effects of self-absorption and pressures higher than 10 atm.

POWER AND IMPEDANCE FOR A CONSTANT-CONDUCTIVITY MODEL
OF THE GAS DISCHARGE

It is important to have an understanding of the basic electromagnetic aspects of coupling that are encountered in using an r-f system to couple power to a highly radiating plasma. In approaching the problem analytically, it is useful to consider a constant-electrical-conductivity, infinite-cylinder model for the plasma since this model allows analysis of the electromagnetic aspects of the problem without detailed consideration of the distribution of the plasma properties. A great deal of work on r-f coupling has been published using this model (e.g., Refs. 4 and 22), but there is need to further generalize this work and to derive new relations that are applicable to small-diameter induction heated plasmas of the type being used to simulate the thermal environment of the nuclear light bulb reactor.

Development of discharge and reactive power relations using both the applied-coil-current approach and the electromagnetic-field approach improves physical understanding of the interaction of the plasma and the electromagnetic fields.* Detailed consideration of a coupling coefficient between dissipative and reactive power is also important since reactive power may be a limit on the performance of an r-f induction heater. Neither a nondimensional coupling coefficient nor the ratio of discharge diameter to coil diameter, r_δ/r_c, have been used generally to describe the addition of power to a gas discharge. Since large discharge power with corresponding high discharge surface radiation flux is an important goal of the experiment in Ref. 2, the effect of discharge and reactive power limits on this flux can be studied using the coupling relation.

To transfer power to a discharge efficiently requires that the impedance of the resonator and discharge be close to the impedance required by the r-f generator. In general, this requires large resistance (of the order of 1000 ohms) and near-zero reactance. Thus, it is desirable to calculate the impedance, the effect of the parameter r_δ/r_c on the impedance, and the frequency shift necessary to minimize the reactance. Knowledge of these factors is particularly important for small values of r_δ/r_c; values of r_δ/r_c between 0.1 and 0.2 are of interest in the experiments of Ref. 2. Finally, the above relations are useful in calculating discharge powers, circuit currents and voltages, frequency shifts, etc., that are encountered with the resonator of Ref. 2.

---

* In a resonating circuit, average discharge power is actual power in the load, and average reactive power is approximately one-half the product of peak sinusoidal current and voltage. These quantities impose limits on resonator design.

Development of Time-Average Discharge and
Reactive Power Equations

The transfer of power from a coil carrying r-f current to a discharge involves the formation of an alternating magnetic field by an applied alternating current. Energy is stored in an alternating magnetic field which, because of its alternating nature, represents an energy flow out of and into the coil. This energy flow per unit time is referred to conventionally as reactive power. In a resonator system, the reactive energy would be stored alternately by the coil and a capacitor. When an electrically conducting medium such as a plasma discharge is present, some of the reactive power is absorbed and there is a net transfer of power out of the coil. The absorbed power is referred to as the dissipative or discharge power. Instantaneous coil power, W, is the product of instantaneous coil current and instantaneous voltage:

$$W = I \, V \tag{13}$$

Assuming sinusoidal time variation of I and V, the expression for coil power consists of a term which has a zero time-average value over one complete cycle (reactive power) and a term which has a nonzero time-average value (discharge power). By taking the absolute value of the reactive power, an average reactive power over a complete cycle can be defined.

For the model shown in Fig. 1 (variations in the radial direction only), the instantaneous coil voltage* is

$$V = N \ell_c \left[- \frac{\partial \phi_c}{\partial t} \right] \tag{14}$$

Here, $\partial \phi_c / \partial t$ is the rate of change of flux linked by the coil:

$$\frac{\partial \phi_c}{\partial t} = \int_0^{r_6} \frac{\partial B_z}{\partial t} \, 2 \pi r \, dr + \int_{r_6}^{r_c} \frac{\partial B_z}{\partial t} \, 2 \pi r \, dr \tag{15}$$

---

* The voltage expression formed here does not include a resistive voltage drop along the coil; this additional voltage drop is not pertinent to the discussion of coupling and can be accounted for separately in analyses of power losses in the r-f system.

16

The first integral in Eq. (15) is integrated over the discharge area where B_z varies with radius and the second is integrated between the discharge and coil where B_z is a constant, B_0. The parameter r_6/r_c is introduced by this process. The details of the integration and the combination of Eqs. (13), (14), and (15) are given in Appendix II. The average power results are

$$\overline{W}_D \doteq \frac{1}{2}\, \omega\, \mu_0 N^2 I_c^2 \pi r_6^2 \ell\, Q \tag{16}$$

and

$$\overline{W}_R = \frac{1}{2}\, \omega\, \mu_0 N^2 I_c^2 \pi r_c^2 \ell \left[1 - \left(\frac{r_6}{r_c}\right)^2 (1 - P) \right] \tag{17}$$

where $\overline{W}_D$ is the discharge power and $\overline{W}_R$ is the reactive power. The functions P and Q are the dimensionless real and imaginary parts, respectively, of the complex flux integral over the discharge area; they are identical to the relations presented in Ref. 4. They are functions of the coupling parameter $\kappa = (\mu_0 \sigma \omega)^{1/2}\, r_6 = (1/\sqrt{2})(d/\delta)$. The variations of P and Q with κ are plotted in Fig. 13.

The result for $\overline{W}_D$ is the same as that obtained in Ref. 4 and elsewhere using a field approach; that is,

$$\overline{W}_D = \int_{vol} \frac{j_\theta^2}{\sigma} \cdot d(vol) \tag{18}$$

The reactive power equation, Eq. (17), is not usually obtained. The flux integration term, P, in Eq. (17) accounts for shielding of the magnetic field from the region of the discharge by induced currents. The field approach can also be used to calculate $\overline{W}_R$:

$$\overline{W}_R = \int_{vol} \vec{H} \cdot \frac{\partial \vec{B}}{\partial t} \cdot d(vol) \tag{19}$$

The integrals in Eqs. (18) and (19) are more complicated to evaluate analytically than the flux integrals in Eq. (15). Thus, the present coil current-voltage approach may also prove useful when end effects, nonuniform conductivity effects, or other complicating factors are treated. The equivalence of the coil current-voltage and field approaches is used in Appendix II, however, to derive the averaging relations for the magnetic field.

17

Ratio of Discharge Power to Reactive Power

The ratio of $\overline{W}_D$ to $\overline{W}_R$ is a nondimensional coupling coefficient, ξ, which characterizes the transfer of power from the coil to the discharge. This coefficient is a function only of κ and r_6/r_c. From Eqs. (16) and (17),

$$\xi \equiv \frac{\overline{W}_D}{\overline{W}_R} = \frac{\left(\frac{r_6}{r_c}\right)^2 Q}{1 - \left(\frac{r_6}{r_c}\right)^2 (1-P)} \tag{20}$$

The variation of the coupling coefficient, ξ, with κ for various values of r_6/r_c is presented in Fig. 14. The dashed line is the locus of the maximum values of ξ. For low values of r_6/r_c, the curves peak at $\kappa = 2.5$. It will be shown later that for $(r_6/r_c) \leq 0.4$, the approximation $\xi \approx (r_6/r_c)^2 Q$ is accurate to better than 10 percent. As r_6/r_c increases, induced currents have a significant effect on total reactive power causing a broadening of the peaks in Fig. 14 and a shifting of the peaks to greater values of κ. For instance, at $r_6/r_c = 1.0$, $\xi = Q/P$, and for large values of κ, ξ approaches 1.0. That is, for tight coupling ($r_6 = r_c$), the limit is $\overline{W}_D = \overline{W}_R$.

The maximum values of ξ that can be obtained for a given value of r_6/r_c, and the corresponding values of κ, are shown in Fig. 15. These curves were obtained by cross-plotting Fig. 14. κ_o is the value of κ for which ξ is a maximum at a given r_6/r_c. The rapid increase of the coupling coefficient with increasing r_6/r_c for large discharges is caused by a rapid decrease in the flux integral, P, and, hence, a decrease in the reactive power, $\overline{W}_R$.

Effect of Reactive and Discharge Power Limits on Discharge Surface Radiation Flux

An important characteristic of an induction heated plasma is the surface radiation flux (see Ref. 2). Both $\overline{W}_R$ and $\overline{W}_D$ affect the radiation flux. A radiation efficiency, η_R, can be defined as $\overline{W}_{RAD}/\overline{W}_D$. Since radiation flux is $\beta_S = \overline{W}_{RAD}/2\pi r_6 \ell$,

$$\beta_S = \left(\frac{\eta_R \overline{W}_D}{2\pi r_c \ell}\right) \frac{1}{r_6/r_c} \tag{21}$$

18

From the definition of the coupling coefficient (Eq. (20)), $\overline{W}_D = \xi \, \overline{W}_R$. For a small discharge (i.e., $r_6/r_c \lesssim 0.4$), the coupling coefficient is approximated by $\xi \approx (r_6/r_c)^2 Q$. Thus,

$$\beta_S = \frac{\eta_R \left(\dfrac{r_6}{r_c}\right) Q \, \overline{W}_R}{2 \pi r_c \ell} \tag{22}$$

To show the effects of $\overline{W}_R$ and $\overline{W}_D$ on β_S, calculations were made for the plasma and coil experiments described in Ref. 2. For these calculations, $r_c = 4$ cm and $\ell = 5$ cm; η_R is assumed equal to 1.0 and the value of κ is assumed equal to 2.5. Since coil winding losses are reduced as r_6/r_c increases, the actual real power available increases, and hence $\overline{W}_D$, increases with increasing values of r_6/r_c. This effect has not been included here. The results of these calculations are presented in Fig. 16. The approximate design operating region for the equipment of Ref. 2 is shown by the shaded portion of Fig. 16. The resonator consists of two coils and corresponding vacuum capacitor assemblies. Each coil-capacitor assembly will support approximately 35 megw of reactive power. Figure 16 indicates that, in maintaining a desired value of β_S, a tradeoff exists between $\overline{W}_R$ and $\overline{W}_D$ as r_6/r_c is varied. In varying r_6/r_c, however, it is also possible to hold the spacing between the coil and discharge, $\Delta = r_c - r_6$, constant as r_6 is varied rather than to hold the coil radius, r_c, constant. A detailed discussion of the effects on β_S of maintaining constant Δ is given in Appendix III. It is shown there that β_S for constant $\overline{W}_R$ always has a maximum at $r_6/r_c \approx 0.5$.

<div align="center">

Coil and Resonator Impedance Relations and
Discussion of Matching Conditions

</div>

Coil Impedance

Exact relations for coil impedance were developed from

$$Z_c = \frac{V_c}{I_c} = \frac{\text{complex} \left\{ N\ell \left[-\dfrac{\partial \phi_c}{\partial t} + I_c R' \right] \right\}}{I_c} \tag{23}$$

where $\partial \phi_c / \partial t$ was developed previously and R' is the coil resistance per turn which produces a resistive voltage drop along the coil. The coil impedance can be put in dimensionless form by dividing by the coil reactance,

<div align="center">

19

</div>

$$z_c = \frac{Z_c}{\omega L_o} = \rho_c + i \mathcal{X}_c \qquad (24)$$

where the unloaded coil inductance is $L_o = \mu_o N^2 \pi r_c^2 \ell_c$. In Appendix IV the resistive and reactive parts of the dimensionless coil impedance are shown to be

$$\rho_c = \frac{R_o}{\omega L_o} + \left(\frac{r_6}{r_c}\right)^2 Q \qquad (25)$$

and

$$\mathcal{X}_c = 1 - \left(\frac{r_6}{r_c}\right)^2 (1 - P) \qquad (26)$$

Figure 17 presents the variations of ρ_c and $\mathcal{X}_c$ with r_6/r_c, assuming $R_o/\omega L_o = 0.002$. This value of $R_o/\omega L_o$ is the approximate value for the experimental coil used in Ref. 2.

Resonator Impedance

The r-f resonator consists of one or more capacitors in parallel with the coil as shown schematically in Fig. 18. From the parallel impedance rule,

$$\frac{1}{Z_r} = \frac{1}{Z_{CAP}} + \frac{1}{Z_c} \qquad (27)$$

or, in dimensionless form,

$$z_R = \frac{Z_R}{\omega L_o} = \frac{1}{\omega L_o} \left[\frac{Z_{CAP} \cdot Z_c}{Z_{CAP} + Z_c} \right] = \rho_R + i\mathcal{X}_R \qquad (28)$$

The resistive and reactive parts of the resonator impedance are derived in Appendix IV. They are

$$\rho_R = \frac{\rho_C}{(1 - \gamma \varkappa_C)^2 + \gamma^2 \rho_C^2} \tag{29}$$

and

$$\varkappa_R = \frac{\varkappa_C (1 - \gamma \varkappa_C) - \gamma \rho_C^2}{(1 - \gamma \varkappa_C)^2 + \gamma^2 \rho_C^2} \tag{30}$$

where $\gamma = (\omega/\omega_o)^2 = \omega^2 L_o C$ is a resonator frequency parameter and ω_o is the unloaded resonant frequency, $\omega_o = 1/(L_o C)^{1/2}$.

The effects of discharge diameter and coupling parameter on resonator impedance are shown in Fig. 19 for the condition $\omega = \omega_o$. The curve of $\kappa = 0$ represents no discharge present; hence at $\omega = \omega_o$ the resonator reactance, $\varkappa_R$, is zero. However, the presence of a small discharge with an optimum value of κ (i.e., $\kappa = 2.5$) reduces the resistive part of the resonator impedance, ρ_R, and causes substantial inductive reactance, $\varkappa_R$, at small values of r_6/r_c. The presence of a large inductive reactance causes an impedance mismatch between the resonator and r-f power amplifier resulting in a poor power transfer efficiency between the resonator and power amplifier.

A resonator is inductive if it is tuned to a frequency below actual resonance; hence a frequency increase should produce a matched condition (i.e., reactive impedance equal to zero). The effect of frequency shift on resonator impedance is shown in Fig. 20. Note that small changes in frequency produce sustantial changes in the impedance curves, particularly in $\varkappa_R$ (Fig. 20b). At some discharge radius ratio, a matching point, $\varkappa_R = 0$,* is indicated for each value of γ. Larger frequency changes shift the matching point to larger values of r_6/r_c. The effects of frequency shift on discharge radius ratio and resonator resistance at the matching points of Fig. 20 are shown in Fig. 21. (Values of γ are related to $\Delta\omega$ and $\Delta\omega/\Delta\omega_o$ in Table I.) Frequency shift here has been expressed as change in frequency relative to unloaded resonator bandwidth, $\Delta\omega/\Delta\omega_o$, where $\Delta\omega_o = R_o/L_o$ and $\Delta\omega = \omega - \omega_o$. For the conditions of Fig. 21, $\omega_o L_o/R_o = 500$; thus $\Delta\omega_o = \omega_o/500 = 2\pi f_o/500$ (for example, at $f_o = 5$ mHz, $\Delta\omega_o = 62,800$ Hz).

---

* This condition assumes that the power supply and transmission line between the supply and resonator are purely resistive which is not necessarily an accurate enough assumption for proper matching. In this case some value of $\varkappa_R$ other than zero could be specified to provide proper matching.

Application of Results to Resonator of Ref. 2

It is of interest to apply the power and impedance relationships derived in the preceding subsections to the resonator described in Ref. 2. This particular resonator was designed so that hundreds of kilowatts of power could be deposited in a plasma approximately 1.0 cm in diameter by 5 cm long. A schematic of the resonator is shown at the top of Table II, and the geometrical and electrical quantities for this resonator are listed below the schematic. Calculations were made for various discharge sizes assuming that coil reactive power, $\overline{W}_R$, was constant and that the matching condition, $\mathcal{X}_R = 0$, always prevailed. Constant reactive power, $\overline{W}_R$, for high values of $\omega L_O/R_O$, can be maintained by holding constant resonator voltage, $V_R = V_c$. It is assumed also that the electrical conductivity of the plasma is constant and equal to 2500 mhos/m. Calculations were performed for three different plasma loads: $r_6 = 0$, 0.5, and 0.79 cm. Table II lists the values of power (real and reactive), coupling coefficients, impedances (resistive and reactive), frequency shifts for match (i.e., reactive resonator impedance equal to zero) and applied currents and voltages for each of the plasma loads. A summary of the equations used and the method for performing calculations is presented in Appendix V.

MAGNETIC PRESSURE ANALYSIS FOR AN R-F DISCHARGE
USING A CONSTANT-CONDUCTIVITY MODEL

The interaction of a circumferential current and an axial magnetic field within a conducting medium will give rise to a force on the conductor normal to the plane formed by the current and magnetic field vectors. In the case of an r-f gas discharge, the induced currents and applied magnetic field will create a pressure gradient in the radial direction. Calculations in Ref. 23 have shown that this pressure gradient and the resulting pressure difference between the center and the edge of the discharge were quite large and, hence, might cause large radial flows in the plasma. However, the approximations used in Ref. 23 could cause the results to be high. Thus, it is desirable to reexamine the magnitude of magnetic pressure that may be expected in plasmas such as those of Refs. 2 and 3.

Calculation of Radial Distribution of Time-Averaged Magnetic Pressure Gradient, $|\vec{j} \times \vec{B}|$

The magnetic pressure gradient is the time-average of the cross product of the induced current and axial magnetic field. An equation for $|\vec{j} \times \vec{B}|$ is derived in Appendix VI. The result in dimensionless form is

$$\frac{|\vec{j} \times \vec{B}|}{B_0^2/\mu_0 r_6} = \left(\frac{j_{\theta_P}}{B_0^2/\mu_0 r_6}\right)\left(\frac{B_{z_P}}{B_0}\right)\left[\frac{\cos(\phi_E - \phi_H)}{2}\right] \tag{31}$$

The relationships for j_{θ_p}, B_{z_p}, ϕ_H and ϕ_E are derived in Appendixes II and VI. Figure 22 presents the radial variations of these quantities. Note that the phase angle difference between current and field at the center of the discharge is always 270 deg; hence the cosine term in Eq. (31) is always zero at the center of the discharge. From the curves of Figs. 22 and 6, Eq. (31) can be evaluated in terms of κ and r/r_6. The effects of these parameters on the dimensionless magnetic pressure gradient are shown in Fig. 23. The magnetic pressure gradient rises sharply near the edge of the discharge.

Calculation of Magnetic Pressure at Center of
Discharge by Graphical Integration

Neglecting changes in the momentum of the plasma, magnetic pressure is given by

$$p_M = \left(p_{CL} - p_{r_6}\right) = \int_{r_6}^{0} \overline{|\vec{j} \times \vec{B}|} \, dr \tag{32}$$

By graphical integration of Fig. 23, the variation of p_M (in dimensionless form) with κ was obtained and the result is shown in Fig. 24. For very large values of κ, the dimensionless magnetic pressure approaches a value of 0.25.

Direct Evaluation of Magnetic
Pressure at Center of Discharge

It is possible to evaluate p_M directly before time-averageing from

$$p_M^* = \int_{r_6}^{0} j_\Theta B_z \, dr \tag{33}$$

where the asterisk indicates a time-varying quantity. Using

$$j_\Theta = -\frac{1}{\mu_0} \frac{dB_z}{dr} \tag{34}$$

one obtains

$$p_M^* = -\frac{1}{\mu_0} \int_{r_6}^{0} \left(\frac{dB_z}{dr}\right) \cdot B_z \cdot dr \tag{35}$$

or

$$p_M^* = -\frac{1}{\mu_0} \int_{r}^{0} B_z \, dB_z \tag{36}$$

24

Equation (36) reduces to

$$p_M^* = \frac{B_z^2|_{r=r_6} - B_z^2|_{r=0}}{2\mu_0} \qquad (37)$$

The time-average value is

$$p_M = \frac{B_{z_p}^2|_{r=r_6} - B_{z_p}^2|_{r=0}}{4\mu_0} \qquad (38)$$

and since $B_{z_p}|_{r=r_6} = B_0$

$$\frac{p_M}{B_0^2/\mu_0} = 0.25\left[1 - \frac{B_{z_p}^2|_{r=0}}{B_0^2}\right] \qquad (39)$$

This checks with Fig. 24.

Application to Conditions of Ref. 2

In Ref. 23, an approximate value of magnetic pressure, p_M, was calculated for a discharge with a nonuniform conductivity distribution using a $|\vec{j} \times \vec{B}|$ distribution approach. The result presented in Ref. 23 is higher by a factor of 470 than the prediction of the uniform-conductivity model discussed here. This discrepancy appears to be the result of inaccuracy in the approximations that were made in Ref. 23. It is concluded that the present solutions give a more realistic estimate of time-averaged magnetic pressure in an r-f discharge.

Applying the present results to the program of Ref. 2, the magnetic energy density, B_0^2/μ_0, can be related to discharge power and the coupling coefficient, ξ, by use of Eq. (17), the relation $I_c = B_0/\mu_0 N$, and the definition of ξ, Eq. (20):

$$\frac{B_0^2}{\mu_0} = \frac{2\overline{W}_D}{\xi\omega\left(\pi r_c^2 \ell\right)\left[1 - \left(\frac{r_6}{r_c}\right)^2(1-P)\right]} \qquad (40)$$

25

For typical conditions of Ref. 2, $\overline{W}_D$ = 600 kw, r_c = 0.5 x 10^{-2} m, ω = $2\pi \dot{x}$ 10^7 rad/sec, κ = 2.5, and $\xi = (r_6/r_c)^2 Q$. The results are $B_o{}^2/\mu_o$ = 1.25 x 10^4 newtons/m^2 and p_M = 0.018 atm. This pressure is small but perhaps not negligible in the discharge momentum equation.

REFERENCES

1. McLafferty, G. H. and H. E. Bauer: Studies of Specific Nuclear Light Bulb and Open-Cycle Vortex-Stabilized Gaseous Nuclear Rocket Engines. United Aircraft Research Laboratories Report F-910093-7, prepared under Contract NASw-847, September 1967. Also issued as NASA CR-1030, 1968.

2. Kendall, J. S., W. C. Roman, and P. G. Vogt: Initial R-F Induction Heating Experiments to Simulate the Thermal Environment of a Nuclear Light Bulb Reactor. United Aircraft Research Laboratories Report G-910091-17, prepared under Contract NASw-847, September 1968.

3. Thorpe, M.: RF Plasma Simulation of Gas Core Reactor. AIAA Paper No. 68-712, presented at the AIAA Fluid and Plasma Dynamics Conference, Los Angeles, California, June 24-26, 1968.

4. Simpson, P. G.: Induction Heating --- Coil and System Design. McGraw-Hill, New York, 1960.

5. Eckert, H. U.: Analytical Solution of the Energy Balance Equation for Thermal Induction Plasmas in Argon. AIAA Paper No. 68-711, presented at the AIAA Fluid and Plasma Dynamics Conference, Los Angeles, California, June 24-26, 1968.

6. Freeman, M. P. and J. D. Chase: Energy Transfer Mechanism and Typical Operating Characteristics for the Thermal Radio-Frequency Plasma Generator. Paper No. 218, presented at the 130th Meeting of the Electrochemical Society, Philadelphia, Pennsylvania , 1967.

7. Soshnikov, V. N. and E. S. Trekhov: The Theory of High-Frequency Vortex Discharges at High Temperature, I. High Temperature, Vol. 4, No. 2, March-April 1966, pp. 165-171.

8. Soshnikov, V. N. and E. S. Trekhov: On the Theory of the High-Frequency Turbulent Discharge at High Temperature, II. High Temperature, Vol. 4, No. 3, May-June, 1966, pp. 318-321.

9. Yos, J. M., private communication of AVCO data published in Ref. 13.

10. Kropp, C. F. and A. B. Cambel: Experimental Determination of the Thermal Conductivity of Atmospheric Argon Plasma. The Physics of Fluids, Vol. 9, No. 5, May 1966, pp. 989-996.

REFERENCES (Continued)

11. Amdur, I. and E. A. Mason: Properties of Gases at Very High Temperatures.
    The Physics of Fluids, Vol. 1, No. 5, September-October, 1958, pp. 370-383.

12. Spitzer, L., Jr. and R. Härm: Transport Phenomena in a Completely Ionized
    Gas. Physical Review, Vol. 89, No. 5, March 1, 1953, pp. 977-981.

13. Devoto, R. S.: Transport Coefficients of Partially Ionized Argon. The Physics
    of Fluids, Vol. 10, No. 2, February 1967, pp. 354-364.

14. Nighan, W., calculations of the properties of argon plasmas, to be published
    in The Physics of Fluids.

15. Olsen, H. N.: Thermal and Electrical Properties of an Argon Plasma. The
    Physics of Fluids, Vol. 2, No. 6, November-December, 1959, pp. 614-623.

16. Weber, R. E. and K. E. Tempelmeyer: Calculation of the D-C Electrical
    Conductivity of Equilibrium Nitrogen and Argon Plasma With and Without Alkali
    Metal Seed. U.S.A.F. AEDC-TDR-64-119, July 1964.

17. McMahon, D. G. and R. Roback: Machine Computation of Chemical Equilibria in
    Reacting Systems. In Kinetics, Equilibria, and Performance of High Temperature
    Systems; Proceedings of the First Conference of Western States Section of the
    Combustion Institute, Los Angeles, California, November 1959 (edited by
    G. S. Bahn and E. E. Zukoski), Butterworths, Washington, 1960.

18. Marteney, P. J., A. E. Mensing, and N. L. Krascella: Experimental Investigation
    of the Spectral Emission Characteristics of Argon - Tungsten and Argon-Uranium
    Induction Heated Plasmas. United Aircraft Research Laboratories Report G-910092-11,
    prepared under Contract NASw-847, September 1968.

19. Gol'dfarb, V. M. and S. V. Dresvin: Optical Investigation of the Distribution
    of Temperature and Electron Density in an Argon Plasma. High Temperature,
    Vol. 3, No. 3, May-June 1965, pp. 303-308.

20. Travers, A.: Experimental Investigation of Peripheral-Wall Injection Techniques
    in a Water Vortex Tube. United Aircraft Research Laboratories Report D-910091-7,
    prepared under Contract NASw-847, September 1965.

21. Dymshits, B. M. and Y. P. Koretskii: An Experimental Investigation of Induced
    Discharges. Soviet Physics - Technical Physics, Vol. 9, No. 9, March 1965,
    pp. 1294-1298.

REFERENCES (Continued)

22. McLachlan, N. W.: Bessel Functions for Engineers. Chapter IX, Oxford University Press, 1934.

23. Chase, J. D.: Magnetic Pressure Phenomena in a RF Induction "Plasma Reactor." AICHE Preprint 9D, presented at the Symposium on High Temperature Technology, New York, November 1967.

24. Adcock, B. D. and W. E. G. Plumtree: On Excitation Temperature Measurements in a Plasma-Jet, and Transition Probabilities for Argon Lines. Journal of Quantitative Spectroscopic Radiative Transfer, Vol. 4, pp. 29-39, 1964.

25. Kraver, T. C.: A Study of Radiation from Argon Plasma. Master of Science Thesis, Department of Aeronautics and Astronautics, M.I.T., February 1961.

26. Stratton, J. A.: Electromagnetic Theory. McGraw-Hill, New York, 1941.

27. Panofsky, W. K. and H. M. Phillips: Classical Electricity and Magnetism. Addison-Wesley, 1955.

LIST OF SYMBOLS

A   Transition probability (used in Appendix I), $\sec^{-1}$

B_z Axial magnetic field induction, $webers/m^2$

B_o Peak value of magnetic field induction in region between coil and discharge, $B_o = \mu_o N I_c$, $webers/m^2$

C   Capacitance, farad

c   Speed of light (used in Appendix I), 3.0×10^8 m/sec

d   Diameter of discharge $2r_6$, cm

$\vec{E}$ Electric field vector, volts/cm

E_ϕ Circumferential electric field, volts/cm

E_n Upper level energy, ev

f   Frequency, Hz

f_o Unloaded resonator frequency, $\dfrac{2\pi}{\sqrt{L_o C}}$, Hz

g   Statistical weight, dimensionless

$\vec{H}$ Magnetic field intensity vector, amp-turn/cm

H_z Axial magnetic field intensity, amp-turn/cm

H_o Peak value of axial magnetic field at $r \geq r_6$, amp-turn/cm

h   Planck constant, (used in Appendix I), 6.62×10^{-34} joule sec

I   Time-dependent coil current, amp

I_c Peak magnitude of coil current, amp

i $\sqrt{-1}$

j_θ Circumferential current density, amp/cm^2

k_B Boltzmann constant, 1.38×10^{-23} joule/deg C

L Inductance, henry

L_O Unloaded coil inductance, $L_O = \mu_O N^2 \pi r_c^2 \ell_c$, henry

ℓ Length of discharge, cm

ℓ_c Length of coil, cm

N Number of coil turns per unit length, cm^{-1}

n_e Number density of electrons, cm^{-3}

P Real part of magnetic field flux integral given in Ref. 4, dimensionless

p Pressure, atm

p_M Time-averaged magnetic pressure increment at center of discharge $p_M = p_{CL} - p_{r_6}$

Q Imaginary part of magnetic field flux integral given in Ref. 4, dimensionless

R_c Effective resistance of coupling coil in presence of discharge, ohms

R_O Unloaded resistance of coil, ohms

R_R Resistive part of resonator impedance, ohms

R' Coil resistance/turn, ohms

r Radius, cm

r_6 Radius of plasma, cm

T Temperature, deg K

t Time, sec

V Time-dependent voltage across coil, volts

V_c — Peak complex magnitude of coil voltage, volts

W — Time-dependent coil power, watts

$\overline{W}_D$ — Time-average power deposited in discharge, watts

$\overline{W}_R$ — Time-average reactive power, watts

$\overline{W}_c$ — Time-average power per unit length conducted, watts/cm

$\overline{W}_{COIL}$ — Time-average power deposited in coil, watts

$\overline{W}_{c_6}$ — Time-average power per unit length conducted out of plasma, watts/cm

$\overline{W}_{RAD}$ — Time-average power per unit length radiated from plasma, watts/cm

$\overline{W}_{CAP}$ — Time-average power stored in capacitor, watts

$\overline{W}_{V_{RAD}}$ — Time-average power per unit volume radiated from plasma, watts/cm^3

X_c — Reactance of coil, ohms

X_R — Reactance of resonator, ohms

Z_c — Complex impedance of coil, ohms

Z_R — Complex impedance of resonator, ohms

Z_0 — Partition function, dimensionless

z_c — Dimensionless coil impedance, $z_c = Z_c/\omega L_0$

z_R — Dimensionless resonator impedance, $z_R = Z_R/\omega L_0$

β_s — Radiation flux at surface of discharge, watts/cm^2

γ — Resonator frequency parameter, $\gamma = (\frac{\omega}{\omega_0})^2$, dimensionless

Δ — Spacing between coil and discharge $\Delta = r_c - r_6$, cm

δ — Skin depth, cm

η_c Coil efficiency, $\overline{W}_D/\left(\overline{W}_D + \overline{W}_{COIL}\right)$

η_R Radiation efficiency, $\overline{W}_{RAD}/\overline{W}_D$, dimensionless

κ Coupling parameter, $\kappa = \dfrac{1}{\sqrt{2}}\,\dfrac{d}{\delta}$, dimensionless

κ_o Value of κ for maximum coupling

λ Thermal conductivity, watts/cm-deg K; or wavelength of light (used in Appendix I), cm

μ_o Permeability of free space, $4\pi \times 10^{-9}$, henry/cm

ξ Dimensionless coupling coefficient between reactive and discharge powers, $\xi = \overline{W}_D/\overline{W}_R$

ρ_c Dimensionless coil resistance, $\rho_c = R_c/\omega L_o$

ρ_R Dimensionless resonator resistance, $\rho_R = R_R/\omega L_o$

σ Electrical conductivity, ohms/cm

ϕ_c Magnetic field flux linked by coil, weber

ϕ_E Phase angle of circumferential electric field, rad

ϕ_H Phase angle of axial magnetic field, rad

χ_c Dimensionless coil reactance, $\chi_c = X_c/\omega L_o$

χ_R Dimensionless resonator reactance, $\chi_R = X_R/\omega L_o$

ω Frequency, radians/sec

$\Delta\omega$ Frequency shift from unloaded resonance, $\Delta\omega = \omega - \omega_o$, rad/sec

$\Delta\omega_o$ Bandwidth of unloaded resonator, $\Delta\omega_o = R_o/L_o$, rad/sec

Subscripts

c   Value at coil

p   Peak value of time-varying quantity

6   Value at edge of plasma, $r = r_6$

CL   Value at center of plasma, $r = 0$

Match   Value of quantity when, $X_c = 0$

Other Notation

$|\ |$ Absolute magnitude of a complex or vector quantity

—   Bar over a quantity indicates a time-average quantity

APPENDIX I

RADIATION FROM AN ARGON PLASMA

Radiation from an argon plasma is due to both line radiation and continuum (or background) radiation. The line radiation is due to bound-bound transitions of the electrons, while continuum radiation is a combination of free-bound and free-free transitions. Line radiation is dominant when plasma temperatures are less than approximately 10,000 deg K while continuum radiation becomes dominant at higher temperatures.

For an argon plasma which is optically transparent and in local thermodynamic equilibrium, the radiation from a line is given by the well-known equation

$$\overline{W}_{V_{RAD_{LINE}}} = \frac{hc}{\lambda} (gA) \frac{n}{Z_0} e^{-E_n/k_B T} \tag{I-1}$$

where $\overline{W}_{V_{RAD_{LINE}}}$ is the radiation in all directions and has the units of w/cm^3 and

n is the number of atoms per unit volume that can contribute to the radiation. For unionized argon, n is the number of neutral atoms (i.e., Ar I). For temperatures less than about 18,000 deg K, the number of doubly ionized argon atoms can be neglected; thus, for singly ionized argon, n is assumed equal to the number of electrons. The variation of the number density of both neutral argon atoms and electrons with temperature was calculated using a computer program patterned after that of Ref. 17. The results of these calculations are presented in Fig. 4 for pressures of 1.0 and 10 atm.

The partition function, Z_0, is assumed equal to 1.0 for Ar I radiation and equal to 5.6 for Ar II radiation. These values are within a few percent of those calculated in Ref. 15.

$\overline{W}_{V_{RAD_{LINE}}}$ was calculated (using Eq. (I-1)) for each of 48 lines of Ar I and 23 lines of Ar II; these values were then summed to obtain the total radiation due to lines, $\sum \overline{W}_{V_{RAD_{LINE}}}$ The gA values used were those listed in Ref. 24. The

where P and Q are the flux integral relations for the discharge region given in Ref. 4. Writing the inner bracket of this last equation as a real part plus an imaginary part and letting $I = \mathcal{R}e\left[I_C e^{i\omega t} \right]$, the power equation

$$W = N \ell_C \, \mathcal{R}e\left\{ I_C e^{i\omega t} \right\} \, \mathcal{R}e\left\{ \left[\omega B_0 \pi r_6^2 Q + i\omega B_0 \pi r_C^2 \left(1 - \frac{r_6^2}{r_C^2}(1-P) \right) \right] e^{i\omega t} \right\} \quad \text{(II-3)}$$

is obtained. This reduces to

$$\text{(II-4)}$$

$$W = \left[\mu_0 N^2 I_C^2 \omega \pi r_6^2 \ell_C Q \right] \cos^2 \omega t - \left[\mu_0 N^2 I_C^2 \omega \pi r_C^2 \ell_C \left(1 - \frac{r_6^2}{r_C^2}(1-P) \right) \right] \sin \omega t \cos \omega t$$

The $\cos^2 \omega t$ term has a time average of 1/2 and is the discharge power of Eq. (16). $\sin \omega t \cos \omega t$ has a zero time average and is the reactive power. By taking an absolute value, an average reactive power level, W_R, can be defined. This introduces a factor of 1/2 and leads to Eq. (17).

According to the field point of view, Ref. 27,

$$W = \int_{VOL} \frac{j^2}{\sigma} d(VOL) + \int_{VOL} \vec{H} \cdot \frac{\partial \vec{B}_z}{\partial t} d(VOL) = \overline{W}_D + \overline{W}_R \quad \text{(II-5)}$$

By direct integration, using relations in Ref. 22, it can be shown that this approach gives results for $\overline{W}_D$ and $\overline{W}_R$ identical to those above. Simpson (Ref. 4) uses j^2/σ to evaluate $\overline{W}_D$, but $\overline{W}_R$ was not obtained. Equating $\overline{W}_D$ and $\overline{W}_R$ from the field approach to $\overline{W}_D$ and $\overline{W}_R$ from the applied current approach, one obtains two averaging relations for B_z:

$$\int_0^{r_C} |\bar{B}_z|^2 \, r \, dr = \mathcal{Im}\left\{ B_0 \int_0^{r_C} i \bar{B}_z r \, dr \right\} \quad \text{(II-6)}$$

$$\mu_0 \sigma \omega \int_0^{r_C} \frac{1}{r^2} \left[\int_0^r |\bar{B}_z| \, r' dr' \right]^2 r \, dr = \mathcal{R}e\left\{ B_0 \int_0^{r_C} i \bar{B}_z r \, dr \right\} \quad \text{(II-7)}$$

APPENDIX III

DISCHARGE SURFACE RADIATION FLUX RELATIONS FOR
CONSTANT SPACING BETWEEN COIL AND DISCHARGE

As one considers a tradeoff between $\overline{W}_D$ and $\overline{W}_R$, maintaining β_s constant as r_6/r_c is varied, it is instructive to maintain constant spacing, Δ, between the coil and the discharge. The value of this spacing might correspond, for example, to a distance required to absorb the radiation β_s in some light absorbing medium. The constant $\overline{W}_D$ and $\overline{W}_R$ relations for β_s, Eqs. (21) and (22), become upon substituting for r_c the relation $r_c = r_6 + \Delta$

$$\beta_s = \frac{\eta_R \overline{W}_D}{2\pi \ell \Delta} \left[\frac{1 - \frac{r_6}{r_c}}{\frac{r_6}{r_c}} \right] \tag{III-1}$$

and

$$\beta_s = \frac{\eta_R Q \overline{W}_R}{2\pi \ell \Delta} \left[\frac{r_6}{r_c} \left(1 - \frac{r_6}{r_c} \right) \right] \text{ for } \frac{r_6}{r_c} < 0.5 \tag{III-2}$$

These equations are sketched qualitatively below.

Discharge -to-coil radius ratio, r_6/r_c

39
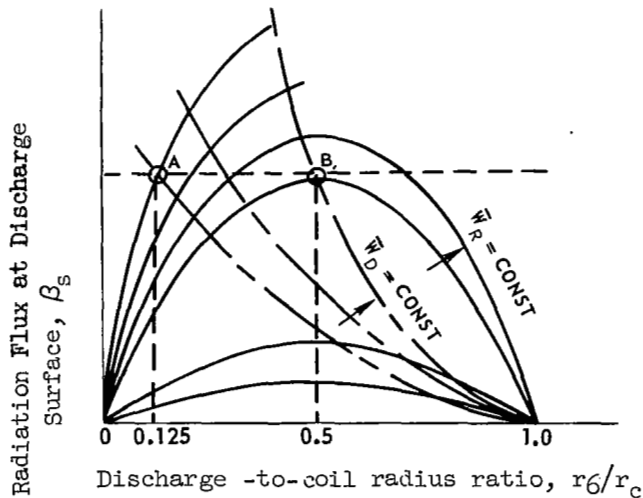
The $\overline{W}_R$ curves given by Eq. (III-2) have maximum β_s values for $r_6/r_c = 0.5$. The $\overline{W}_R$ and $\overline{W}_D$ curves approach zero as r_6/r_c approaches unity since r_c approaches infinity. The exact curves, with the exact relation for optimum coupling valid for $r_6/r_c > 0.5$, will peak just above r_6/r_c of 0.5.

Two coil and discharge geometries are shown in (A) and (B) below. These correspond to the operating points (A) and (B) in the above sketch.

(A): $r_6/r_c = 0.125$ (B): $r_6/r_c = 0.5$
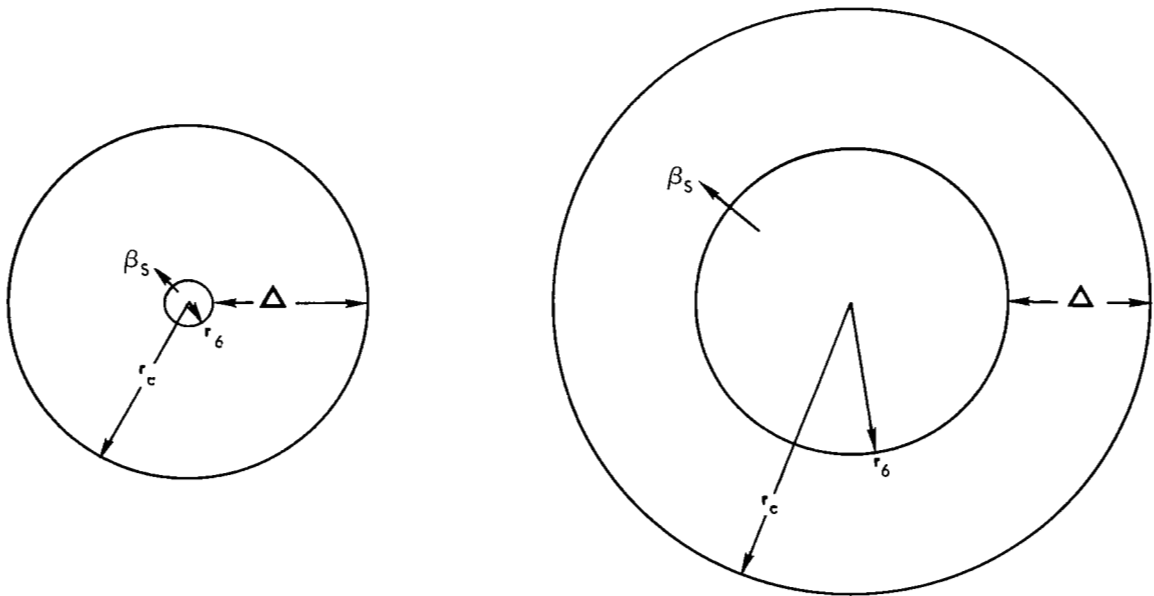
In this comparison, $\beta_{s_{(A)}} = \beta_{s_{(B)}}$ and $\Delta_{(A)} = \Delta_{(B)}$. Thus $(r_c)_{(B)} / (r_c)_{(A)} = 1.75$ and, from Eqs. (III-1) and (III-2), $(\overline{W}_R)_{(B)} / (\overline{W}_R)_{(A)} = 0.44$ and $(\overline{W}_D)_{(B)} / (\overline{W}_D)_{(A)} = 7.0$, respectively. This shows that some saving in $\overline{W}_R$ can be achieved by using a large r_6/r_c to obtain a specified β_s; however, a very large increase in $\overline{W}_D$ is required. It would not be worthwhile to increase r_6/r_c above 0.5.

Finally, since $r_c = \dfrac{\Delta}{\Delta/(1 - (r_6/r_c))}$, note that specification of β_s and r_6/r_c therefore specifies $\overline{W}_R$, $\overline{W}_D$, and r_c.

40

APPENDIX IV

DERIVATION OF COIL AND RESONATOR IMPEDANCES

Deviation of the dimensionless coil impedance relation z_c in Eq. (24) requires evaluation of the coil voltage relation

$$V_C = \text{complex mag} \left\{ N \ell_C \left[- \frac{\partial \phi_C}{\partial t} + I_C R' \right] \right\} \qquad \text{(IV-1)}$$

This can be done using Eq. (II-2) for $\frac{\partial \phi_C}{\partial t}$ with $B_0 = \mu_0 N I_C$. Current I_C then cancels out in the impedance definition, Eq. (23), and by defining $L_0 = \mu_0 N^2 \pi r_c^2 \ell_c$, the desired dimensionless form can be obtained.

Derivation of Resonator Impedance, z_R

According to the parallel rule for addition of impedances, the resonator model (Fig. 18) has an impedance given by

$$\frac{1}{Z_R} = \frac{1}{Z_C} + \frac{1}{(1/i\omega C)} \qquad \text{(IV-2)}$$

or

$$Z_R = \frac{Z_C / i \omega C}{1/i \omega C + Z_C}$$

which reduces to

$$Z_R = \frac{Z_C}{1 + i \omega C Z_C} \qquad \text{(IV-3)}$$

Now Z_C can be written as

$$Z_C = \omega L_0 z_C \qquad \text{(IV-4)}$$

41

Introducing Eq. (IV-4) into Eq. (IV-3), dividing by ωL_0 and defining a dimensionless resonator impedance

$$z_R \equiv \frac{Z_R}{\omega L_0} = \rho_R + i \chi_R \tag{IV-5}$$

yields the relation

$$z_R = \frac{z_C}{1 + i(\omega^2 L_0 C) z_C} \tag{IV-6}$$

Here, $\gamma = \omega^2 L_0 C$, introduces a parameter characterizing the operation of the resonator. A value $\gamma = 1.0$ corresponds to the unloaded resonant frequency of the resonator, $\omega_0 = \frac{1}{\sqrt{L_0 C}}$; hence, $\gamma = (\frac{\omega}{\omega_0})^2$.

Equation (IV-6) can be written as the sum of real and imaginary parts. Since $z_C = \rho_C + i \chi_C$, then

$$z_R = \frac{\rho_C + i \chi_C}{1 + i \gamma (\rho_C + i \chi_C)} \tag{IV-7}$$

Expanding the denominator and taking its complex conjugate gives

$$z_R = \frac{(\rho_C + i \chi_C)\left[(1 - \gamma \chi_C) - i \gamma \rho_C\right]}{\left[(1 - \gamma \chi_C) + i \gamma \rho_C\right]\left[(1 - \gamma \chi_C) - i \gamma \rho_C\right]} \tag{IV-8}$$

which reduces to the desired form, Eqs. (29) and (30):

$$z_R = \left[\frac{\rho_C}{(1 - \gamma \chi_C)^2 + \gamma^2 \rho_C^2}\right] + i \left[\frac{\chi_C(1 - \gamma \chi_C) - \gamma \rho_C^2}{(1 - \gamma \chi_C)^2 + \gamma^2 \rho_C^2}\right] \tag{IV-9}$$

CALCULATION PROCEDURE FOR QUANTITIES PRESENTED IN TABLE II

Values in Table II have been obtained using relations given in the report. The relations used are identified and the procedure employed are discussed in this Appendix.

The circuit parameters listed in Table II correspond to one of the two coil-capacitor assemblies of the resonator employed in the experiments of Ref. 2. Unloaded coil inductance, L_0, has been calculated from the relation

$$L_0 = \mu_0 N^2 \pi r_c^2 \ell_c \qquad (V-1)$$

Resonator capacitance is a given quantity and unloaded resonator frequency, f_0, is

$$f_0 = \frac{\omega_0}{2\pi} = \frac{1}{2\pi\sqrt{L_0 C}}$$

The unloaded resonator "Q" factor represents a typical "Q" factor for the resonator of Ref. 2. Unloaded coil resistance (winding resistance) R_0 is then

$$R_0 = \frac{"Q"}{\omega_0 L_0} = \frac{"Q"}{2\pi f_0 L_0} \qquad (V-2)$$

Unloaded resonator bandwidth, Δf_0, is given by the relation that

$$\Delta f_0 = \frac{f_0}{"Q"} \qquad (V-3)$$

Hence,

$$\frac{f_0}{\Delta f_0} = "Q" \qquad (V-4)$$

The discharge conductivity shown in Table II is the design value of Ref. 2 and skin depth is given by the relation shown in Table II.

The basic input parameter held constant for the calculation is coil reactive power, $\overline{W}_R$. For the resonator of Ref. 2 coil reactive power would be maintained constant by maintaining constant resonator voltage, V_R, i.e., constant capacitor reactive power. It is assumed that the match condition of zero resonator reactance would be maintained by adjustment of frequency.

The parameter varied in Table II is discharge radius, r_6, or equivalently the ratio of discharge radius to coil radius, r_6/r_c. The unloaded resonator is specified as $r_6 = 0$. The three finite discharge sizes shown represent (1) a typical small

discharge, $r_6/r_c = 0.125$, (2) a discharge giving the value of κ for maximum Q, $\kappa = 2.50$ (note that this is not maximum ξ for $r_6/r_c = 0.125$ (Fig. 14)) and (3) a typical large discharge, $r_6/r_c = 0.50$.

The coefficient ξ is obtained from Fig. 14, or from Eq. (20) using values of P and Q for the appropriate values of κ from Fig. 13. Discharge power is then simply $\overline{W}_D = \xi \overline{W}_R$.

Dimensionless coil reactance, χ_c and resistance, ρ_c, are obtained from Fig. 17 or Eqs. (25) and (26). Actual coil reactance X_c and resistance R_c are obtained from

$$X_c = \left(\omega L_0\right) \chi_c \qquad \text{(V-5)}$$

$$R_c = \left(\omega L_0\right) \rho_c \qquad \text{(V-6)}$$

where $\omega \approx \omega_0$ is sufficiently accurate here.

Frequency shift, $f-f_0$, necessary to establish the resonator matching condition, $X_R = 0$, can be obtained by setting the numerator of Eq. (30) equal to zero, i.e.,

$$\chi_c \left(1 - \gamma \chi_c\right) - \gamma \rho_c^2 = 0 \qquad \text{(V-7)}$$

or, at match,

$$(\gamma)_{match} = \frac{\chi_c}{\chi_c^2 + \rho_c^2} \qquad \text{(V-8)}$$

Since

$$\gamma = \omega^2 L_0 C = \left(\frac{\omega}{\omega_0}\right)^2 = \left(\frac{f}{f_0}\right)^2 \approx 1 + \frac{2(f-f_0)}{f_0} \qquad \text{(V-9)}$$

or

$$(f-f_0) = \frac{f_0}{2}\left(\gamma - 1\right) \qquad \text{(V-10)}$$

The ratio $\dfrac{\Delta\omega}{\Delta\omega_0} = \dfrac{\Delta f}{\Delta f_0}$ is then determined using the given value of Δf_0.

Resonator resistance is determined from Eq. (29). By direct substitution of the $(\gamma)_{match}$ relation into Eq. (29), it follows that $(\rho_R)_{match} = (\chi_c^2 + \rho_c^2)/\rho_c$. Note that due to the coil winding resistance, R_0, unloaded resonator reactance is not quite zero when $\omega = \omega_0 = \dfrac{1}{\sqrt{L_0 C}}$, but is very small relative to R_R.

Peak coil current is determined from the reactive power relation

$$\overline{W}_R = \frac{1}{2} X_C I_C{}^2 \qquad\qquad (V-11)$$

Hence

$$I_C = \left(\frac{2\overline{W}_R}{X_C}\right)^{1/2} \qquad\qquad (V-12)$$

Coil peak voltage, V_C, is determined by the relation

$$V_C = I_C |Z_C| \qquad\qquad (V-13)$$

where $|Z_C| = (R_C{}^2 + X_C{}^2)^{1/2}$ is the magnitude of coil impedance.

Power stored in the capacitor is then

$$\overline{W}_{CAP} = \frac{1}{2} \omega C V_C{}^2 \qquad\qquad (V-14)$$

Now for matched conditions, it was seen that $\gamma_{match} = \omega^2 L_0 C = \dfrac{X_C}{X_C{}^2 + \rho_C{}^2}$; this leads to the relation $(\omega C)_{match} = \dfrac{X_C}{X_C^2 + R_C^2}$, or

$$\qquad\qquad (V-15)$$

But

$$\overline{W}_{CAP} = \frac{1}{2}\left(\frac{X_C}{X_C{}^2 + R_C{}^2}\right) V_C{}^2 \qquad\qquad (V-16)$$

Hence,

$$\frac{V_C{}^2}{R_C{}^2 + X_C{}^2} = I_C{}^2 \qquad\qquad (V-17)$$

$$\overline{W}_{CAP} = \frac{1}{2} X_C I_C{}^2 = \overline{W}_R \qquad\qquad (V-17)$$

Thus, at match, the reactive power stored by the capacitor is the same as that stored by the coil. Thus $\overline{W}_{CAP} = 35 \times 10^6$ here and is also shown separately in Table II. Note also that $\overline{W}_{CAP}$ can be given by

$$\overline{W}_{CAP} = \frac{1}{2} V_C |I_C - I_R| \qquad\qquad (V-18)$$

where $|I_C - I_R|$ is the peak value of current through the capacitor.

Power dissipated in the coil windings, $\overline{W}_{COIL}$, is given by

$$\overline{W}_{COIL} = \frac{1}{2} I_C{}^2 R_0 \qquad\qquad (V-19)$$

45

where R_O is the winding resistance of the coil. A coupling efficiency can be defined as

$$\eta_c = \frac{\overline{W}_D}{\overline{W}_{COIL} + \overline{W}_D} \qquad (V-20)$$

Since resonator reactance is zero, resonator current, I_R, is in phase with V_R (also V_C) and total power, $\overline{W}_D + \overline{W}_{COIL}$, is

$$\overline{W}_D + \overline{W}_{COIL} = \frac{1}{2} I_R V_R = \frac{1}{2} I_R V_C \qquad (V-21)$$

Hence,

$$I_R = \frac{2\left(\overline{W}_D + \overline{W}_{COIL}\right)}{V_C} \qquad (V-22)$$

Magnetic pressure, P_M, was determined from Fig. 24 and Eq. (40).

46

DERIVATION OF MAGNETIC PRESSURE GRADIENT

Axial B and azimuthal j combine to produce a radial magnetic pressure gradient given here by

$$\left| \vec{j} \times \vec{B} \right| = j_\theta B_z \tag{VI-1}$$

where the positive direction in Fig. 1 is radially outwards by the right-hand rule. Introducing complex sinusoidal notation for j and B,

$$\left| \vec{j} \times \vec{B} \right| = Re\left\{ j_{\theta_P} e^{i\left(\phi_E + \omega t\right)} \right\} Re\left\{ B_{z_P} e^{i\left(\phi_H + \omega t\right)} \right\} \tag{VI-2}$$

Taking the time average of this last expression yields the desired magnetic pressure gradient relation given in dimensionless form as Eq. (31). It follows from the relation for B, Eq. (II-1), that

$$\frac{B_{z_P}}{B_0} = \frac{\left(ber^2 \kappa \frac{r}{r_6} + bei^2 \kappa \frac{r}{r_6} \right)^{1/2}}{\left(ber^2 \kappa + bei^2 \kappa \right)^{1/2}} \tag{VI-3}$$

and

$$\phi_H = \tan^{-1}\left(\frac{bei\, \kappa \frac{r}{r_6}}{ber\, \kappa \frac{r}{r_6}} \right) - \tan^{-1}\left(\frac{bei\, \kappa}{ber\, \kappa} \right) \tag{VI-4}$$

Finally, since $j_\theta = -\left(\frac{1}{\mu_0 r_6} \right)\left(\frac{\partial B_z}{\partial \frac{r}{r_6}} \right)$,

$$\frac{j_{\theta_P}}{B_0 / \mu_0 r_6} = \frac{\kappa\left[ber'^2\left(\kappa \frac{r}{r_6} \right) + bei'^2\left(\kappa \frac{r}{r_6} \right) \right]^{1/2}}{\left(ber^2 \kappa + bei^2 \kappa \right)^{1/2}} \tag{VI-5}$$

and

$$\phi_E = \pi + \tan^{-1}\left(\frac{\text{bei}'\kappa \frac{r}{r_6}}{\text{ber}'\kappa \frac{r}{r_6}}\right) - \tan^{-1}\left(\frac{\text{bei}\,\kappa}{\text{ber}\,\kappa}\right) \tag{VI-6}$$

These last relations have been evaluated and the results are shown in Figs. 6 and 23.

TABLE I

RELATION OF FREQUENCY PARAMETER TO
FREQUENCY SHIFT FROM UNLOADED RESONANCE
AND THE UNLOADED RESONATOR BANDWIDTH

$$\gamma = (\omega/\omega_o)^2 \approx \left[1 + 2\Delta\omega/\omega_o\right] \doteq \left[1 + 2\,(R_o/\omega L_o)\,\Delta\omega/\Delta\omega_o\right]$$

$\Delta\omega = \omega - \omega_o$, $f_o = \omega_o/2\pi = 5.0$ mHz, $\Delta f_o = \Delta\omega_o/2\pi = 0.01$ mHz, $\Delta f_o/f_o = R_o/L_o = 0.002$

Frequency Parameter, γ	Bandwidth Ratio, $\Delta\omega/\Delta\omega_o$	Frequency Shift From Resonance, $\Delta f = \Delta\omega/2\pi$, Hz
1.0000	0.0	0
1.0004	0.1	1,000
1.0020	0.5	5,000
1.0100	2.5	25,000
1.0400	10.0	100,000
1.1000	25.0	250,000

49

TABLE II

PARAMETERS FOR RESONATOR OF REF. 2

(See Appendix V for Calculation Procedure)

SKETCH OF RESONATOR
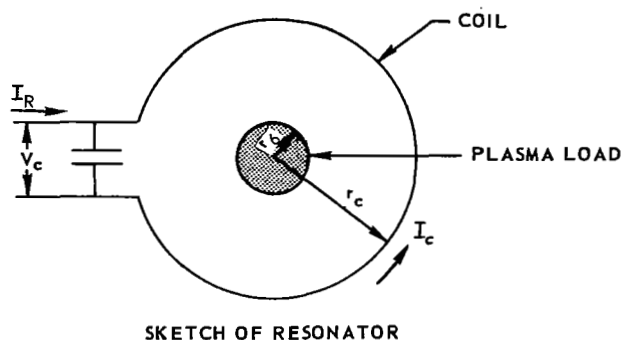
Circuit Parameters

Coil radius, r_c = 4 cm
Coil length, ℓ_c = 3.2 cm
Discharge length, ℓ = 3.2 cm
Coil turns/length, $N = 1/\ell_c$ = 0.31 turns/cm
Unloaded coil inductance, $L_o = \mu_o N^2 \pi r_c^2 \ell_c$ = 0.20 x 10^{-6} henry
Resonator capacitance, C = 4.5 x 10^{-9} farad
Unloaded resonator resonant frequency, $f_o = \omega_o/2\pi$ = 5.3 x 10^6 Hz
Unloaded coil impedance, $\omega_o L_o$ = 6.70 ohm
Unloaded resonator "Q" factor, "Q" $= \omega_o L_o/R_o$ = 500
Unloaded coil resistance (winding resistance), R_o = 0.013 ohm
Unloaded resonator bandwidth, Δf_o = 10,600 Hz

Discharge Properties

Electrical conductivity, σ = 2500 mhos/m
Electrical skin depth, $\delta = \sqrt{\dfrac{2}{\mu_o \sigma \omega_o}}$ = 0.44 cm

Basic Input Parameter

Coil reactive power, $\overline{W}_R$ = 35 x 10^6 w

50

TABLE II (Continued)

Parameter	Unloaded Resonator	Loaded Resonator		
Discharge Radius, r_6 - cm	0	0.5	0.78	2.0
Ratio of discharge radius to coil radius, r_6/r_c	0	0.125	0.195	0.500
Coupling parameter, $\kappa = \frac{1}{\sqrt{2}} \frac{2r_6}{\delta}$	0	1.60	2.50	6.40
Coupling coefficient, ξ	0	0.0044	0.0142	0.060
Discharge power, $\overline{W}_D$ - w	0	0.154×10^6	0.497×10^6	2.10×10^6
Dimensionless coil reactance, x_c	1.00	0.998	0.986	0.807
Coil reactance, X_c - ohms	6.70	6.68	6.60	5.40
Dimensionless coil resistance, ρ_c	0.002	0.006	0.016	0.052
Coil resistance, R_c - ohms	0.0134	0.043	0.170	0.348
Value of frequency parameter, γ, for matching	1.000	1.001	1.015	1.232
Frequency shift for matching, $f-f_o$ - Hz	0	2.6×10^3	39.8×10^3	615.0×10^3
Ratio of frequency shift for matching to unloaded bandwidth, $(f-f_o)/\Delta f_o = \Delta\omega/\Delta\omega_o$	0	0.25	3.75	58.0
Dimensionless resonator reactance, x_R	-1.00	0	0	0
Resonator reactance, X_R - ohms	-6.70	0	0	0
Dimensionless resonator resistance, ρ_R	500	166	61	12.5
Resonator resistance, R_R - ohms	3340	1110	410	84
Peak coil current, I_c - amps	3240	3243	3260	3600
Peak coil voltage, V_c - volts	21.7×10^3	21.7×10^3	21.5×10^3	19.5×10^3
Reactive power on capacitor, $\overline{W}_{CAP}$ - w	35×10^6	35×10^6	35×10^6	35×10^6
Power dissipated in coil windings, $\overline{W}_{COIL}$ - w	70.0×10^3	70.2×10^3	71.3×10^3	87.0×10^3
Overall coupling efficiency, $\eta_c = \overline{W}_D/(\overline{W}_{COIL} + \overline{W}_D)$	0	0.69	0.88	0.96
Resonator current, I_R - amps	6.5	20.7	52.4	225.0
Magnetic pressure, p_M - atm	0	0.005	0.018	0.039

FIG. 1

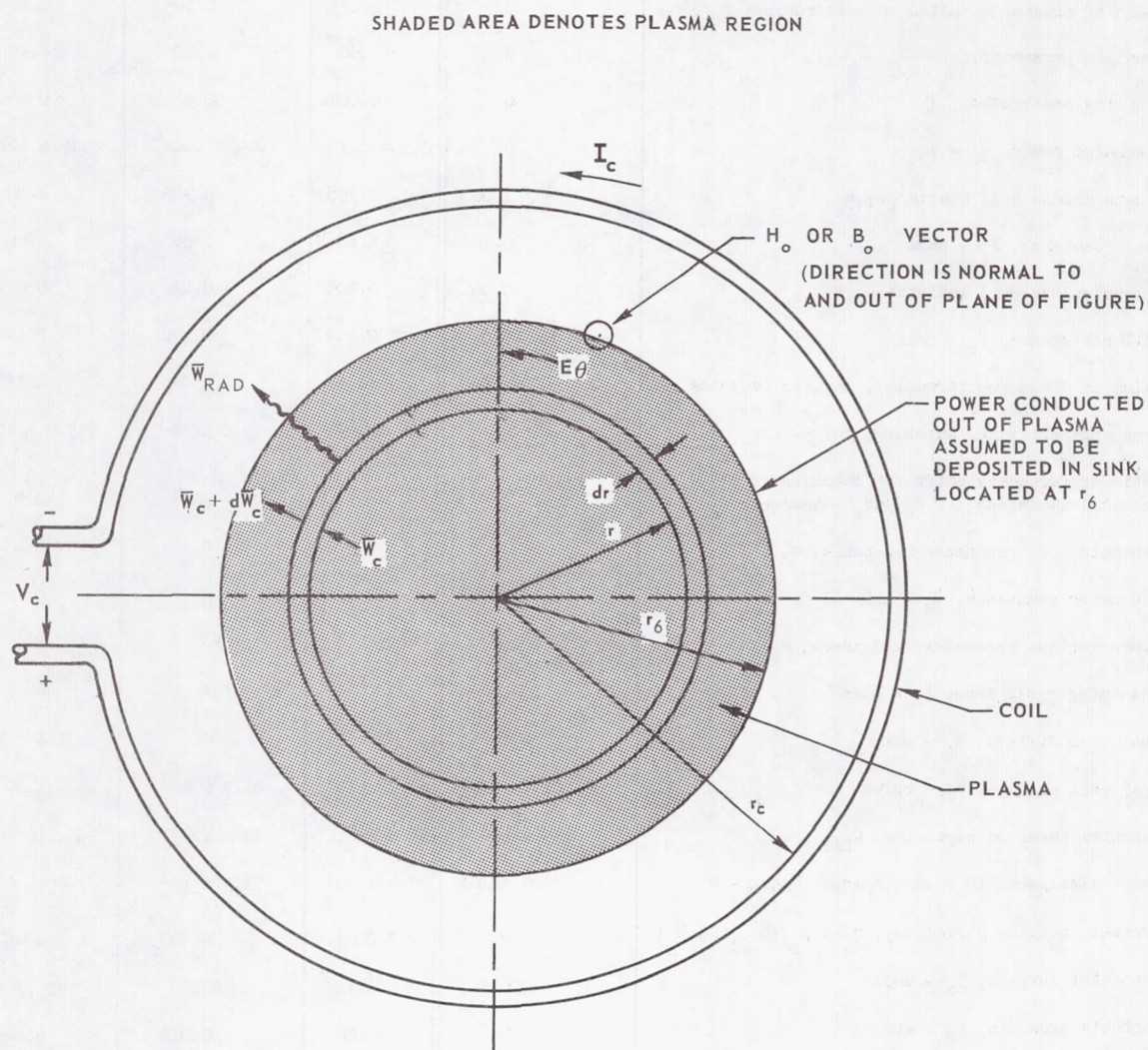# SKETCH OF ONE-DIMENSIONAL MODEL USED IN COMBINED ELECTROMAGNETIC AND THERMAL ANALYSIS OF R-F DISCHARGES

SHADED AREA DENOTES PLASMA REGION

I_c

H_o OR B_o VECTOR
(DIRECTION IS NORMAL TO
AND OUT OF PLANE OF FIGURE)

$\overline{W}_{RAD}$

$E\theta$

POWER CONDUCTED
OUT OF PLASMA
ASSUMED TO BE
DEPOSITED IN SINK
LOCATED AT r_6

$\overline{W}_c + d\overline{W}_c$

$\overline{W}_c$

dr
r

$-$

V_c

r_6

$+$

COIL

PLASMA

r_c

FIG. 2

VARIATION OF ARGON THERMAL CONDUCTIVITY WITH TEMPERATURE

PRESSURE = 1 ATM

SYMBOL OR LINE	SOURCE	TYPE OF INVESTIGATION
O	REF. 9	EXPERIMENTAL
△	REF. 10	EXPERIMENTAL
——— ———	REF. 11	THEORETICAL
— —— —	REF. 12	THEORETICAL
— — — —	REF. 13	THEORETICAL

SOLID LINE DENOTES VARIATION ASSUMED IN THIS REPORT

THERMAL CONDUCTIVITY, λ – W/CM – DEG K

TEMPERATURE, T – DEG K

53
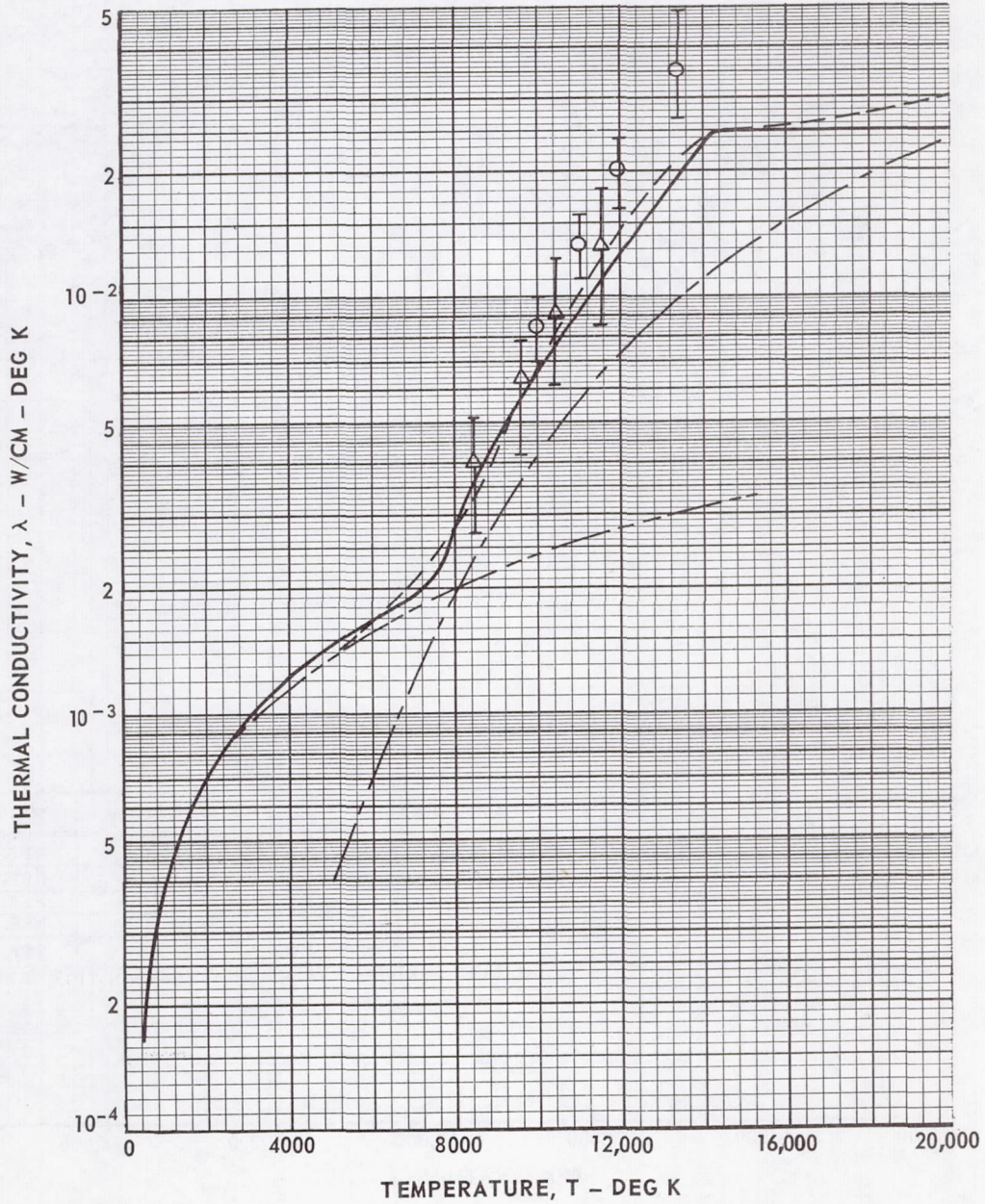
FIG. 3

VARIATION OF ARGON ELECTRICAL CONDUCTIVITY WITH TEMPERATURE

SYMBOL OR LINE	PRESSURE-ATM	SOURCE
– – – – – – –	1.0	REF. 14
—————	10.0	REF. 14
—·—·—·—	1.1	REF. 15
—··—··—··	1.0	REF. 16
··············	1.0	REF. 13

SOLID LINE DENOTES VARIATION ASSUMED IN THIS REPORT
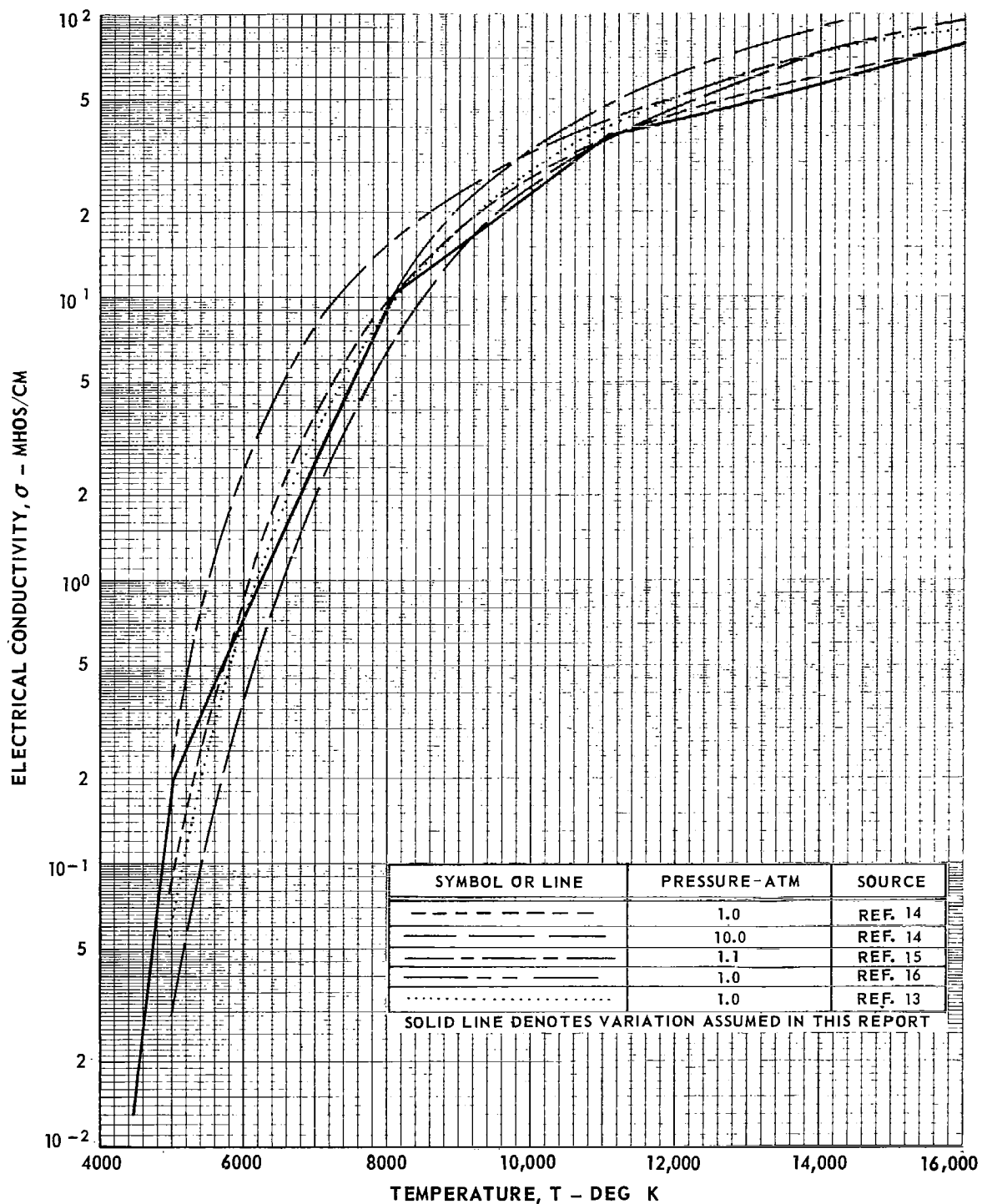
FIG. 4

EFFECT OF TEMPERATURE ON ARGON COMPOSITION

CALCULATED USING MODIFIED METHOD OF REF. 17

———————— NEUTRAL ATOMS

— — — — ELECTRONS
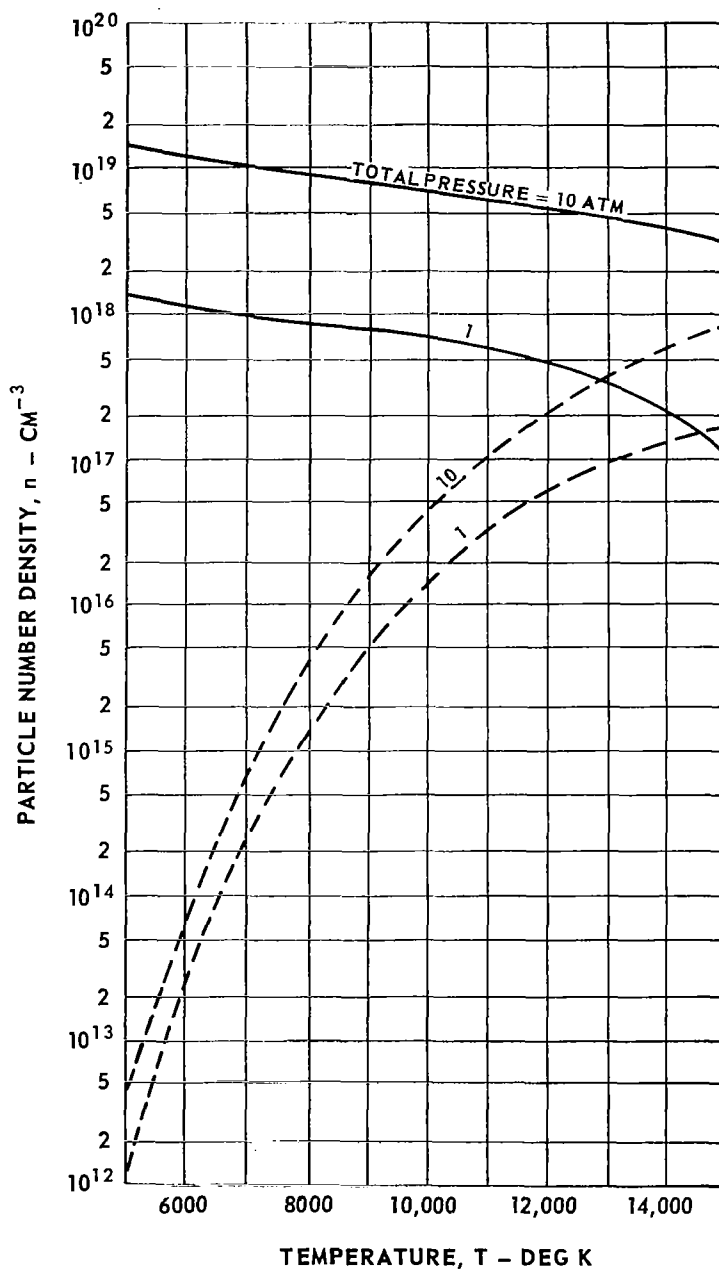
FIG. 5

VARIATION OF POWER RADIATED WITH TEMPERATURE FOR ARGON

CALCULATED USING METHOD OF APPENDIX I

◯ DATA AT p ≃ 1 ATM FROM REF. 18

FIG. 6
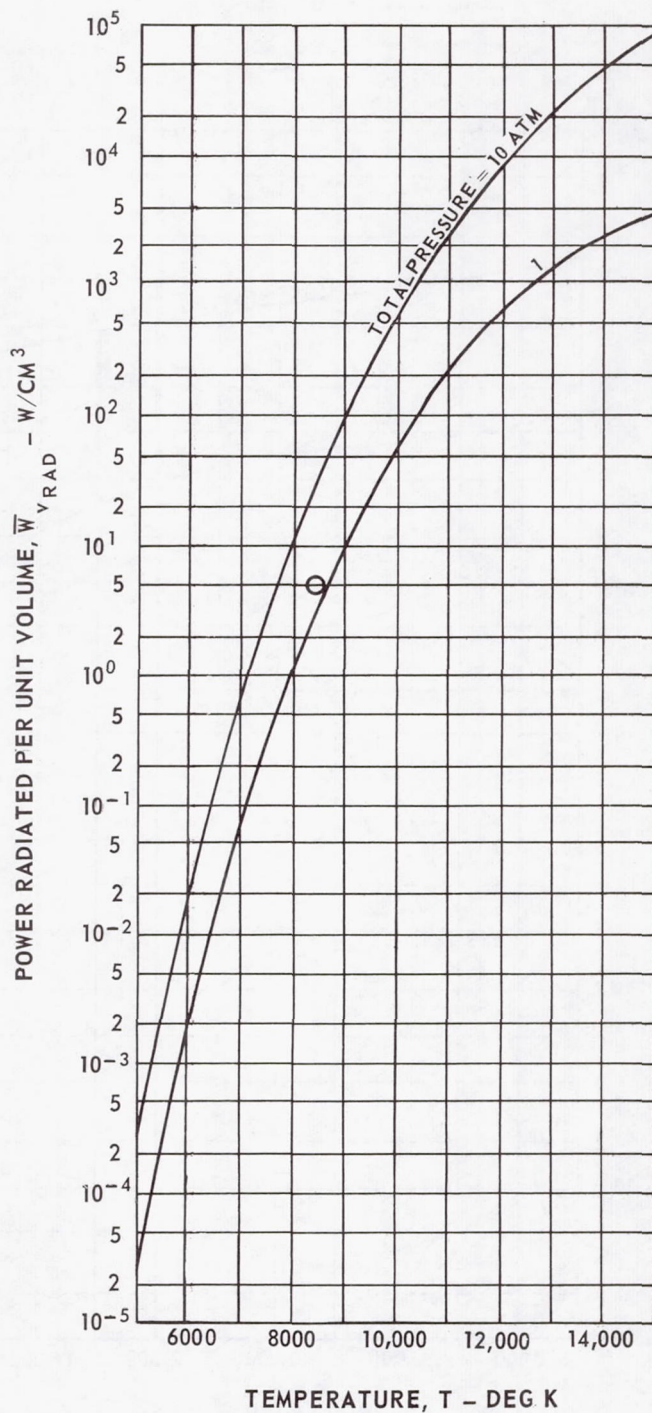
TYPICAL COMPARISONS OF RADIAL DISTRIBUTIONS OF AXIAL MAGNETIC FIELD CALCULATED USING EXACT AND NUMERICAL METHODS

COMPARISONS MADE FOR CONSTANT ELECTRICAL CONDUCTIVITY
AND NO THERMAL CONDUCTION OR RADIATION

$$K = \frac{1}{\sqrt{2}} \frac{d}{\delta}$$

CALCULATION PROCEDURE	LINE OR SYMBOL	K	d/δ	TYPICAL VALUES OF PARAMETERS TO PROVIDE SPECIFIED d/δ			
				f – MHZ	σ–MHO/CM	δ –CM	d –CM
EXACT ANALYTICAL METHOD	————	2.0	2.83	10	25	0.32	0.9
	– – – –	4.0	5.66	10	25	0.32	1.8
NUMERICAL METHOD	□	2.0	2.83	10	25	0.32	0.9
	○	4.0	5.66	10	25	0.32	1.8

Y-axis: AXIAL MAGNETIC FIELD AT RADIUS r , $\dfrac{H_z \rho}{H_o}$

AXIAL MAGNETIC FIELD AT RADIUS r_6

X-axis: $\dfrac{\text{RADIUS FROM CENTER OF DISCHARGE}}{\text{RADIUS OF DISCHARGE}}$, $\dfrac{r}{r_6}$
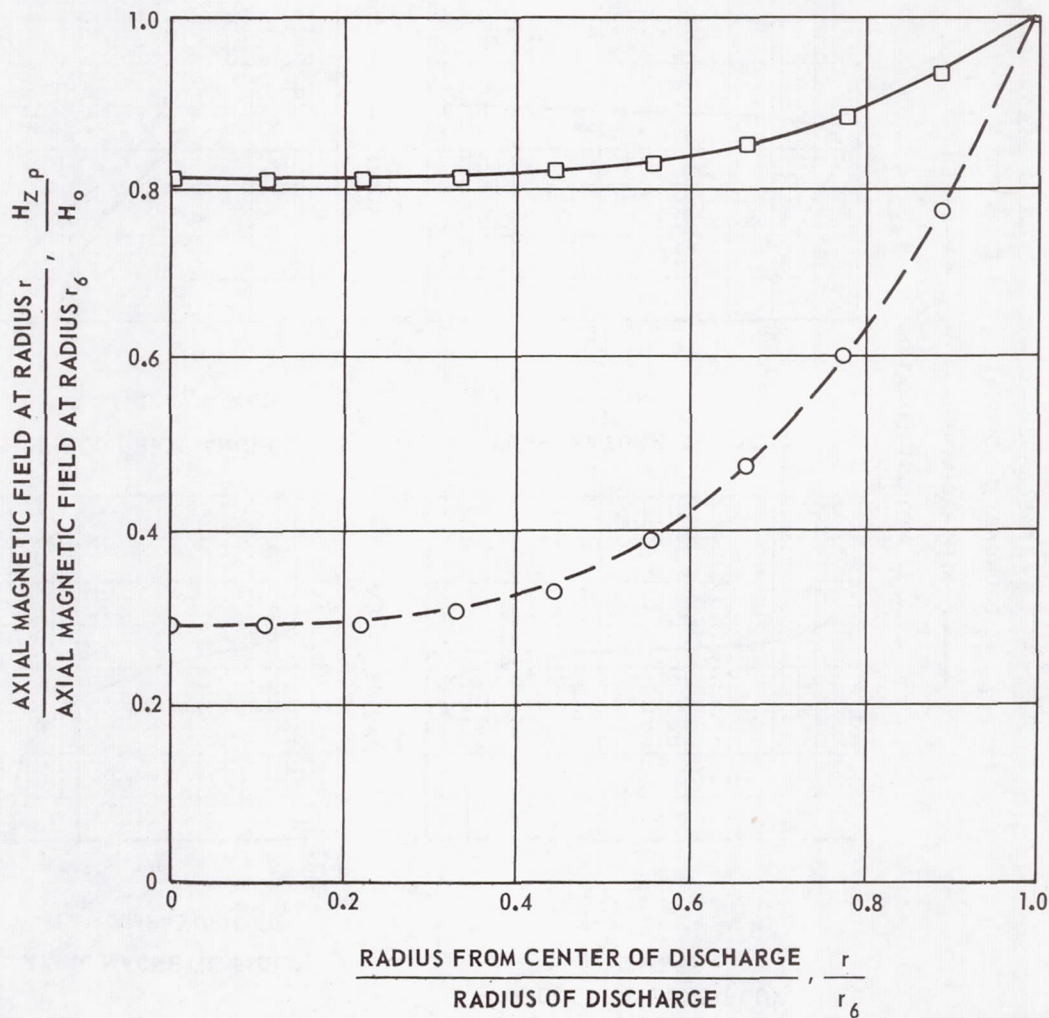
TYPICAL THEORETICAL RADIAL VARIATIONS OF TEMPERATURE, HEAT FLUX, AND ELECTRIC
AND MAGNETIC FIELDS IN AN INDUCTION HEATED PLASMA WITH AND WITHOUT RADIATION TERMS

FREQUENCY = 10 MHZ   ARGON PRESSURE = 1.0 ATM

BOUNDARY CONDITIONS: T_{CL} = 10,000 K $H_{Z_{CL}}$ = 5 AMP TURNS/CM

—————— WITH RADIATION: $\overline{W}_{RAD}$ = 1140 W/CM $\overline{W}_D / \ell$ = 3270 W/CM

— — — — WITHOUT RADIATION: $\overline{W}_{RAD}$ = 0 $\overline{W}_D / \ell$ = 153 W/CM
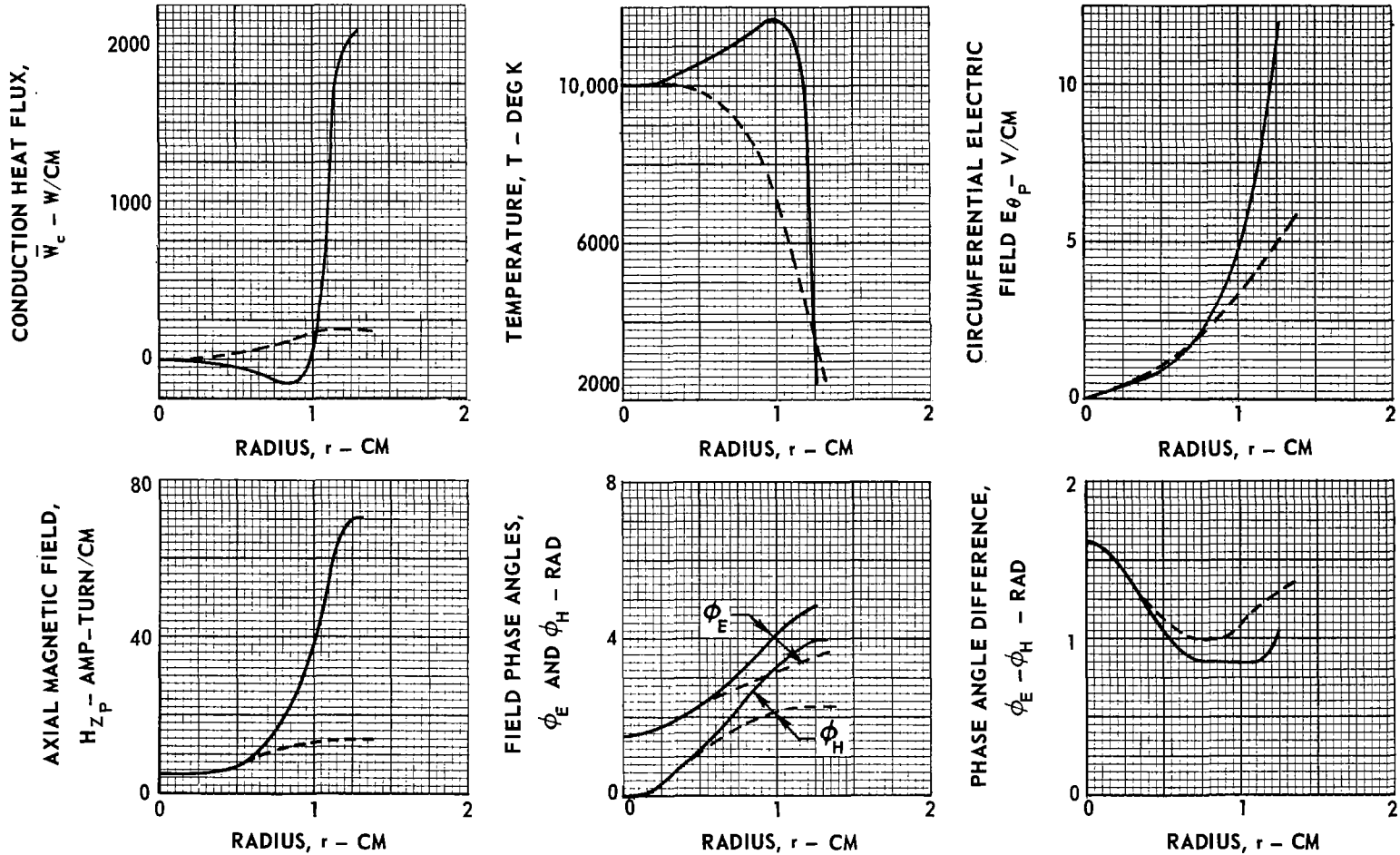
FIG. 7

58

FIG. 8

EFFECTS OF PLASMA RADIUS AND AXIAL MAGNETIC FIELD ON POWER CONDUCTED AND RADIATED FROM ARGON PLASMA AT 1.0–ATM PRESSURE

FREQUENCY = 10^7 HZ

━━━━━━ CURVES OF CONSTANT r_6

━━ ━━ CURVES OF CONSTANT T_{CL}

━━━━━━ CURVES OF CONSTANT $\overline{W}_{RAD}$

AXIAL MAGNETIC FIELD EXTERNAL TO PLASMA, H_o – AMP–TURNS/CM

POWER CONDUCTED FROM PLASMA, $\overline{W}c_6$ – W/CM

FIG. 9

EFFECTS OF PLASMA RADIUS AND AXIAL MAGNETIC FIELD ON POWER CONDUCTED AND RADIATED FROM ARGON PLASMA AT 10–ATM PRESSURE

FREQUENCY = 10^7 HZ

CURVES OF CONSTANT r_6

CURVES OF CONSTANT T_{CL}

CURVES OF CONSTANT $\overline{W}_{RAD}$

POWER CONDUCTED FROM PLASMA, $\overline{W}_{c_6}$ – W/CM

AXIAL MAGNETIC FIELD EXTERNAL TO PLASMA, H_o – AMP–TURNS/CM
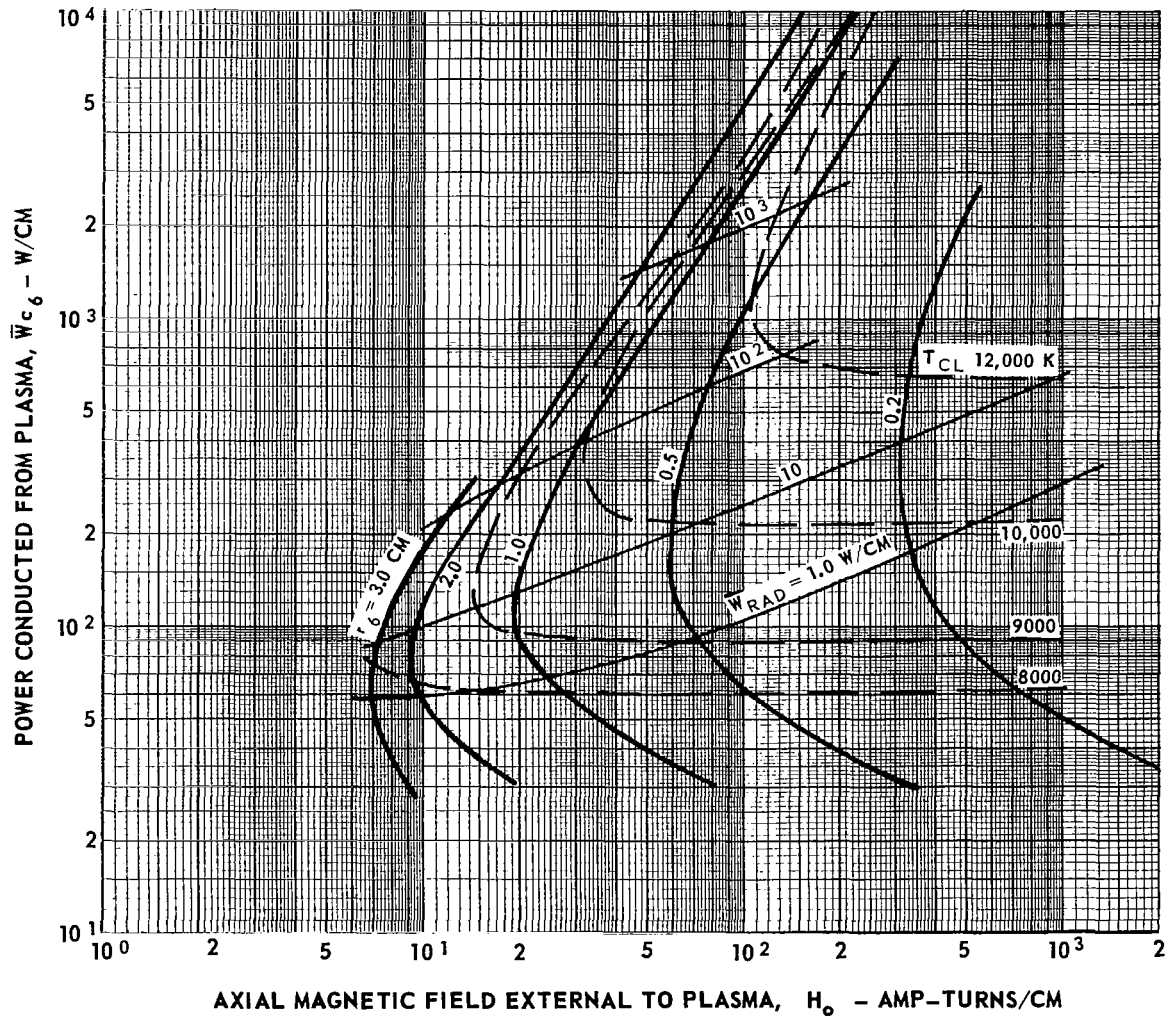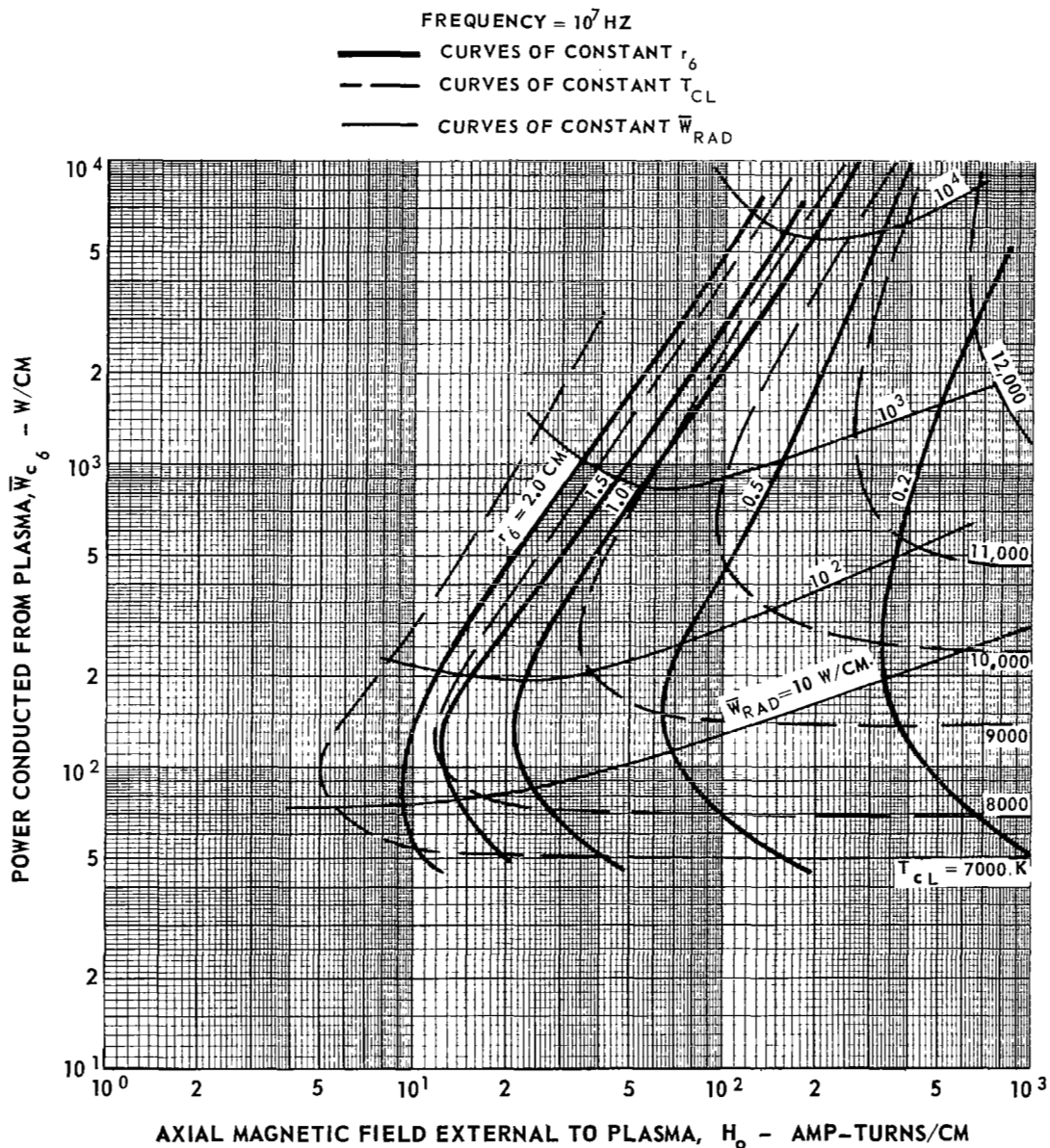
FIG. 10

EFFECT OF PLASMA RADIUS AND AXIAL MAGNETIC FIELD ON TOTAL POWER DEPOSITED IN PLASMA, RADIATION EFFICIENCY, AND EQUIVALENT COUPLING PARAMETER FOR ARGON PLASMA AT 1.0-ATM PRESSURE

FREQUENCY = 10^7 MHZ

IN CROSS-HATCHED AREA NO EQUIVALENT COUPLING PARAMETER CAN BE DEFINED

———— CURVES OF CONSTANT r_6

— — — CURVES OF CONSTANT η_R

— — — CURVES OF CONSTANT κ_{eq}

O   DATA FROM REF. 18 (SEE TEXT)

AXIAL MAGNETIC FIELD EXTERNAL TO PLASMA, H_o —AMP-TURNS/CM
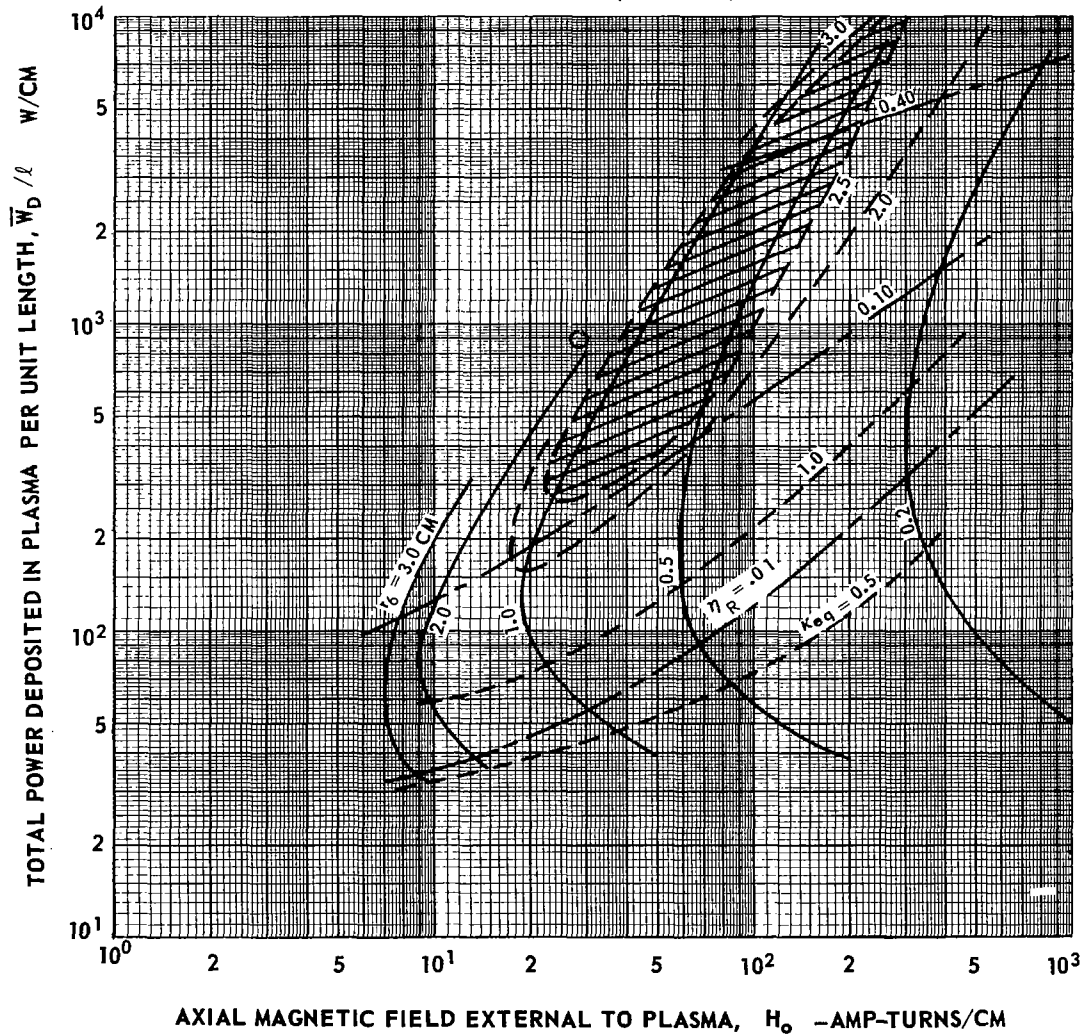
FIG. 11

EFFECTS OF PLASMA RADIUS AND AXIAL MAGNETIC FIELD ON TOTAL POWER DEPOSITED IN PLASMA, RADIATION EFFICIENCY, AND EQUIVALENT COUPLING PARAMETER FOR AN ARGON PLASMA AT 10–ATM PRESSURE

FREQUENCY $= 10^7 H_Z$
IN CROSS–HATCHED AREA NO EQUIVALENT COUPLING PARAMETER CAN BE DEFINED
————— CURVES OF CONSTANT r_6
—— — —— CURVES OF CONSTANT κ_{eq}
—— — — —— CURVES OF CONSTANT η_R

FIG. 12
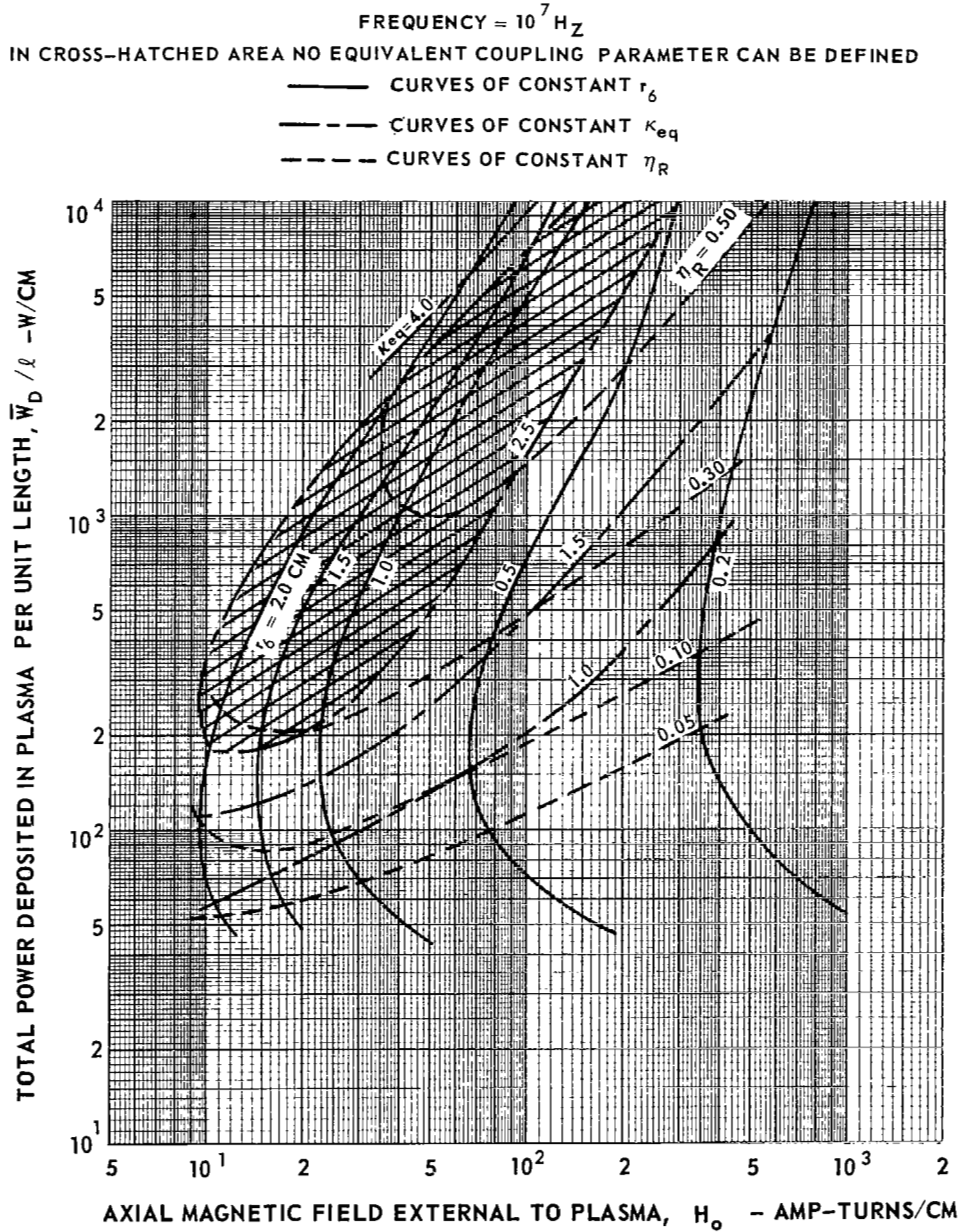
VARIATION OF PLASMA SKIN DEPTH WITH ELECTRICAL CONDUCTIVITY

$$\delta = \frac{1}{\sqrt{\pi \mu_o f \sigma}}$$
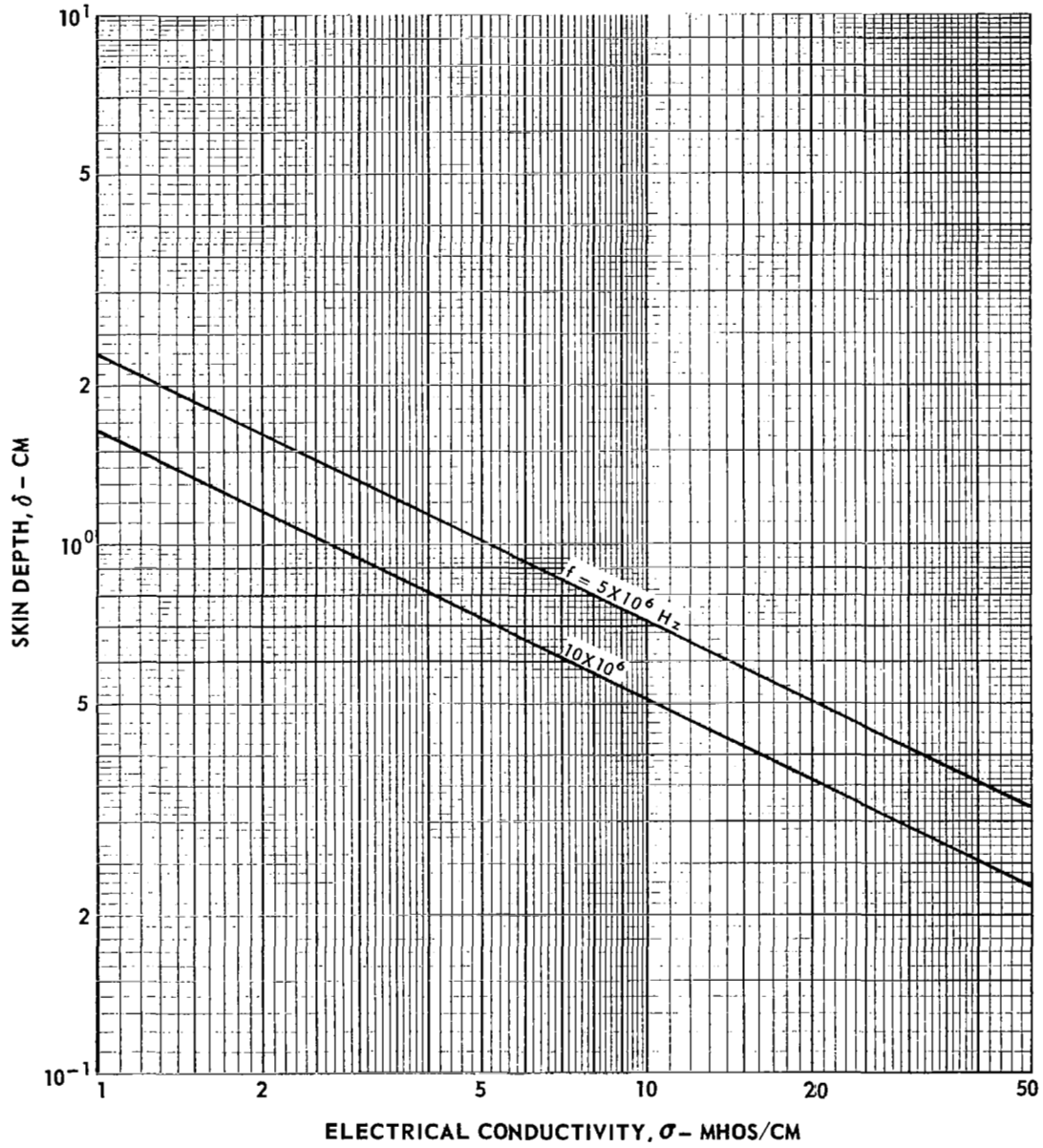
EFFECT OF COUPLING PARAMETER ON DIMENSIONLESS MAGNETIC FIELD FLUX INTEGRAL RELATIONS

$$K = \frac{1}{\sqrt{2}} \frac{d}{\delta}$$

$\sigma = $ CONSTANT

P AND Q IDENTICAL TO RELATIONS GIVEN IN REF. 4
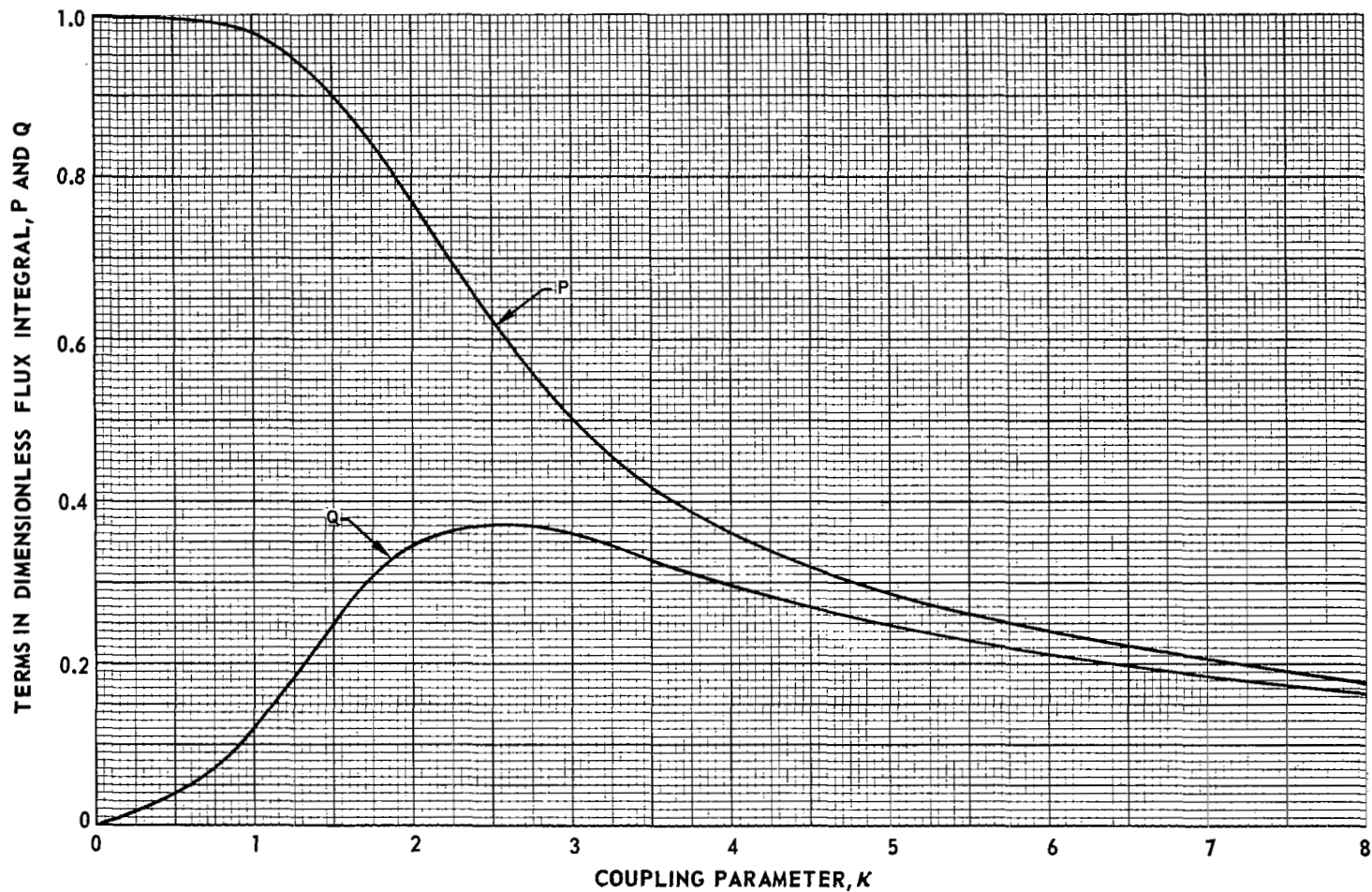
FIG. 13

FIG. 14

EFFECT OF DISCHARGE SIZE AND COUPLING PARAMETER ON THE RATIO OF TOTAL DISCHARGE POWER TO REACTIVE POWER

σ = CONSTANT

$\kappa = \dfrac{1}{\sqrt{2}}\dfrac{d}{\delta}$

DASHED LINE DENOTES LOCUS OF MAXIMUM VALUES OF ξ

COUPLING PARAMETER, K – DIMENSIONLESS

FIG. 15
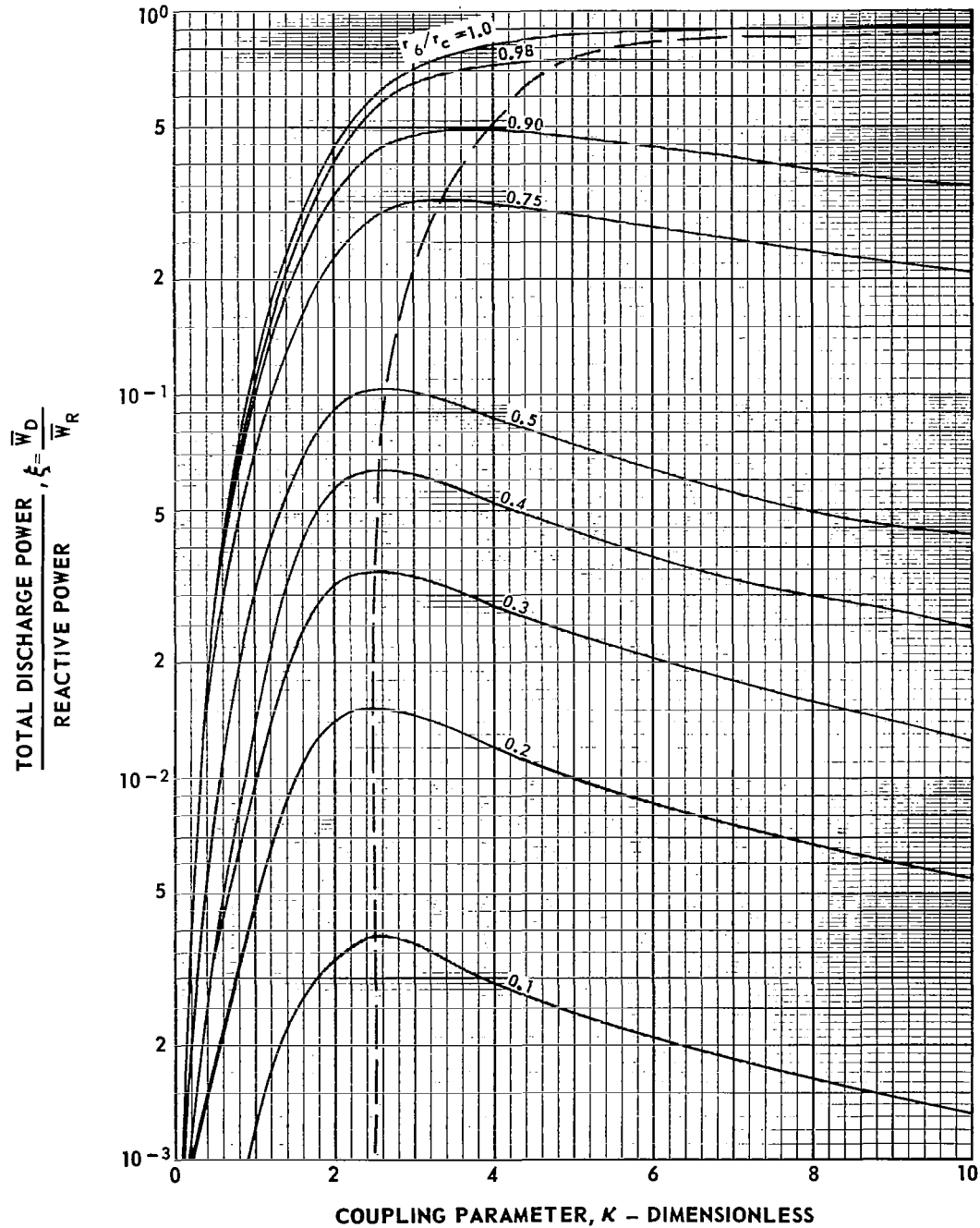
VARIATION OF MAXIMUM $\overline{W}_D/\overline{W}_R$ AND CORRESPONDING COUPLING PARAMETER WITH DISCHARGE SIZE

CROSSPLOT OF DASHED CURVE ON FIG.14

$\sigma =$ CONSTANT

a) MAXIMUM $\overline{W}_D/\overline{W}_R$
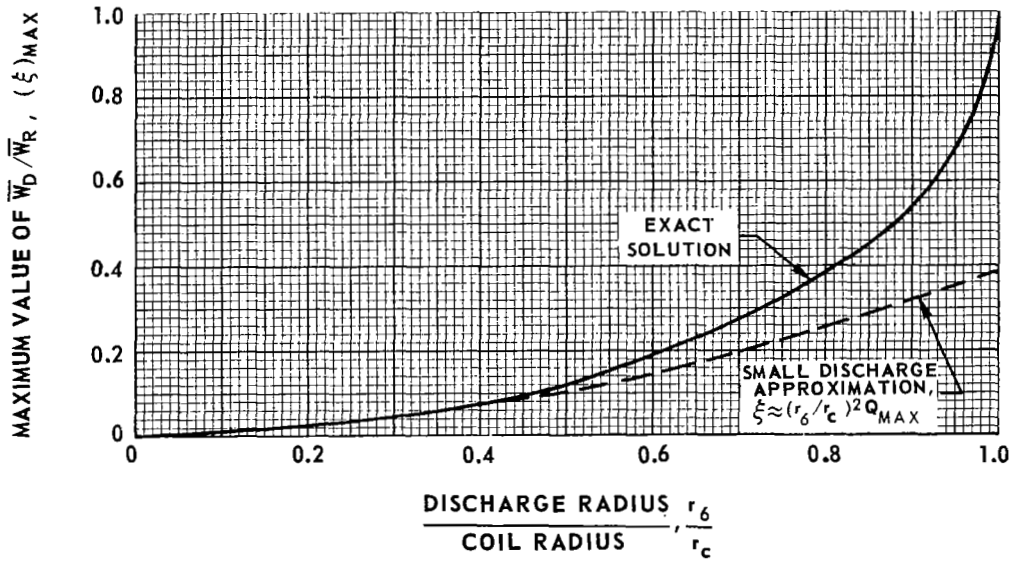
b) COUPLING PARAMETER FOR MAXIMUM COUPLING

FIG. 16
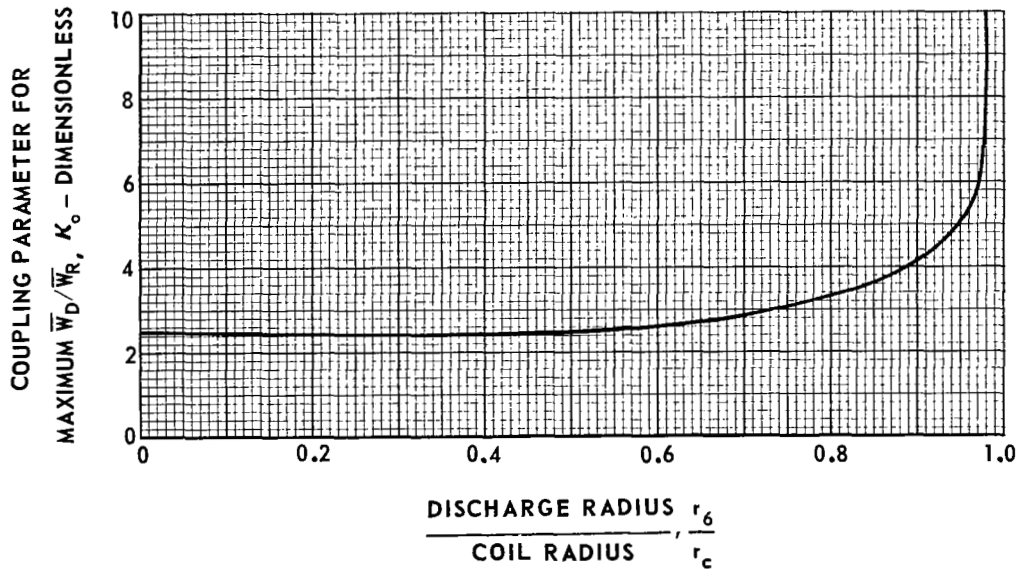
EFFECT OF DISCHARGE SIZE ON DISCHARGE SURFACE RADIATION FLUX FOR VARIOUS DISCHARGE AND REACTIVE POWER LEVELS

$r_c = 4.0$ CM, $\ell = 5.0$ CM, $\eta_R = 1.0$

CROSS—HATCHED REGION DENOTES A TYPICAL SYSTEM ENVELOPE OF OPERATION

$\sigma = $ CONSTANT

FIG. 17
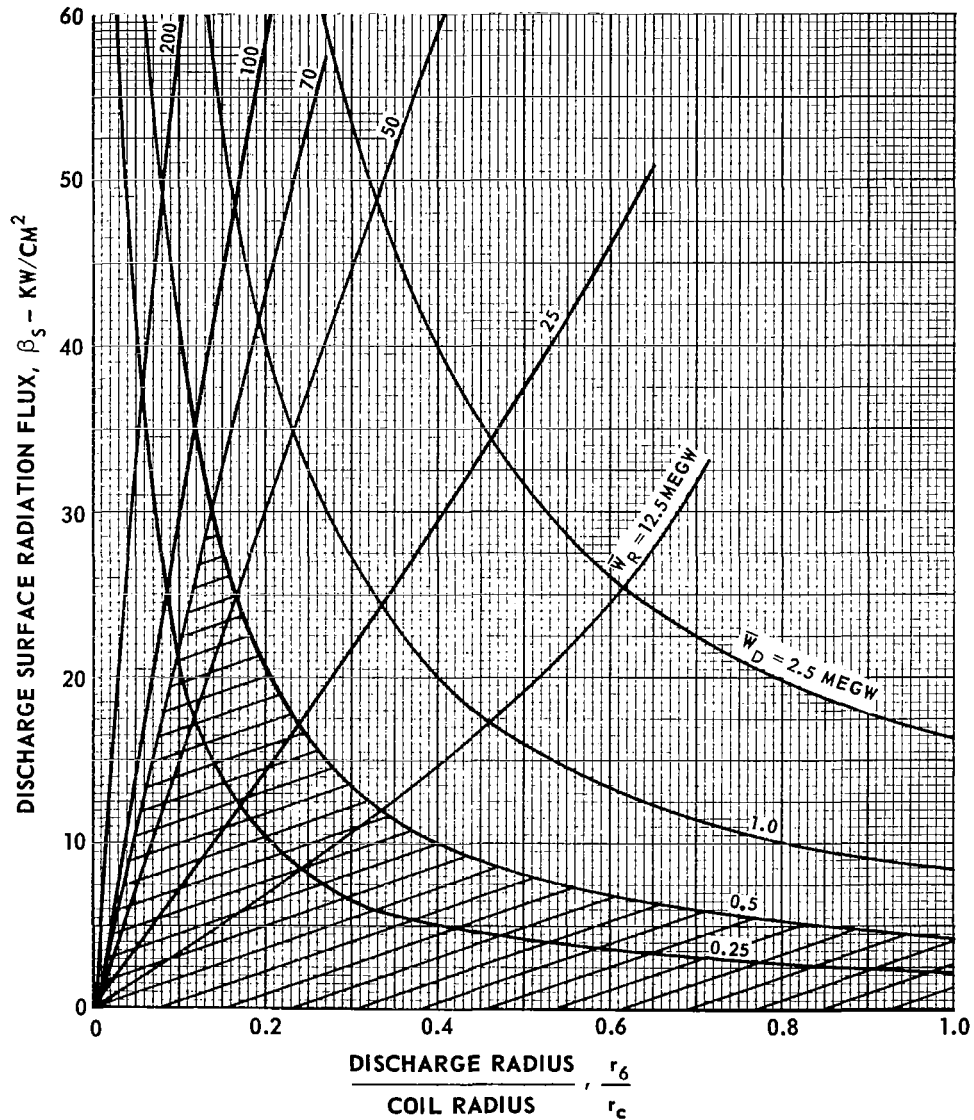
EFFECT OF DISCHARGE SIZE AND COUPLING PARAMETER ON COIL IMPEDANCE

$$\kappa = \frac{1}{\sqrt{2}} \frac{d}{\delta} \qquad \sigma = \text{CONSTANT}$$

a) COIL RESISTANCE

$$\rho_c = \frac{R_c}{\omega L_o}$$

$K = 3.0$
2.0
5.0
1.0
0

DISCHARGE RADIUS , $\dfrac{r_6}{r_c}$
COIL RADIUS

DIMENSIONLESS COIL RESISTANCE, ρ_c

b) COIL REACTANCE

$$\chi_c = \frac{X_c}{\omega L_o}$$

$K = 0$ 1.0
2.0
3.0
5.0

DIMENSIONLESS COIL REACTANCE, χ_c

DISCHARGE RADIUS $\dfrac{r_6}{r_c}$
COIL RADIUS

FIG. 18
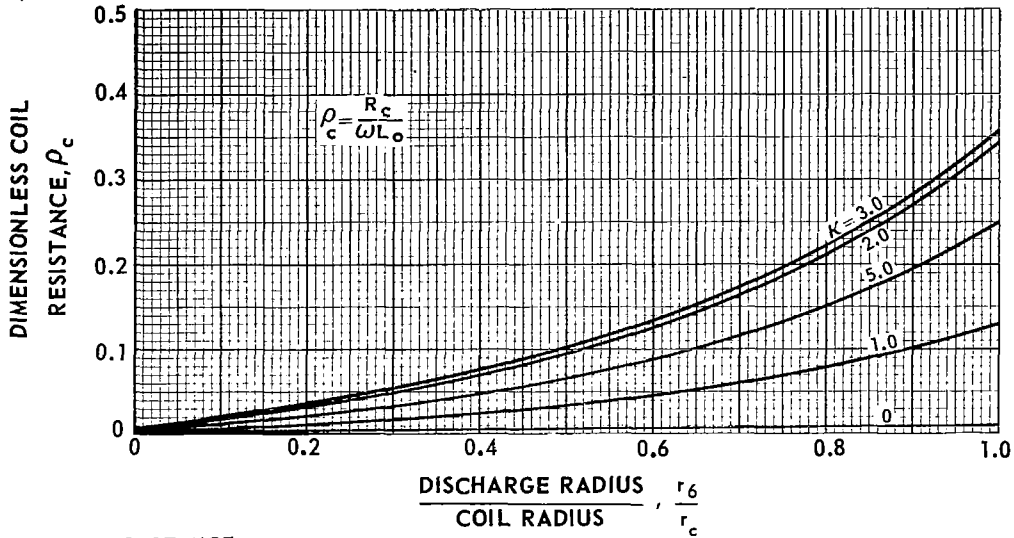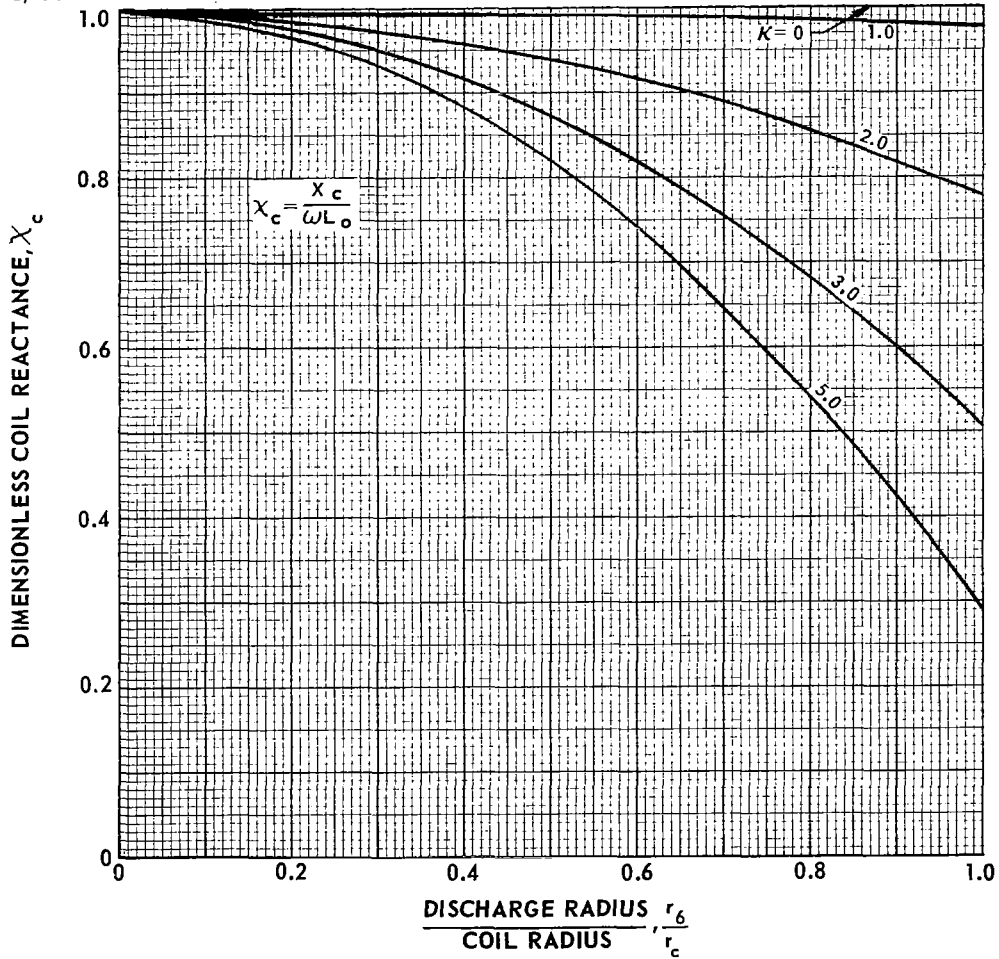
CIRCUIT MODEL FOR RESONATOR

$$\frac{Z_c}{\omega L_o} = \rho_c + i X_c$$

$$V_c = V_R$$

RESONATOR MODEL, IMPEDANCE Z_R

69

FIG. 19
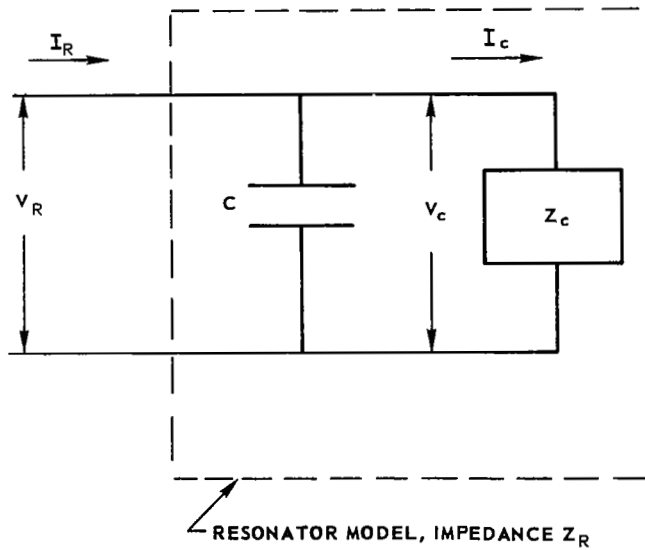
TYPICAL MISMATCH CONDITION CAUSED BY DISCHARGE WHEN RESONATOR FREQUENCY IS MAINTAINED AT UNLOADED RESONANCE VALUE

$$K = \frac{1}{\sqrt{2}} \frac{d}{\delta}, \quad \sigma = \text{CONSTANT}, \quad f = f_o = \omega_o / 2\pi = 5.0 \text{ MHZ}$$

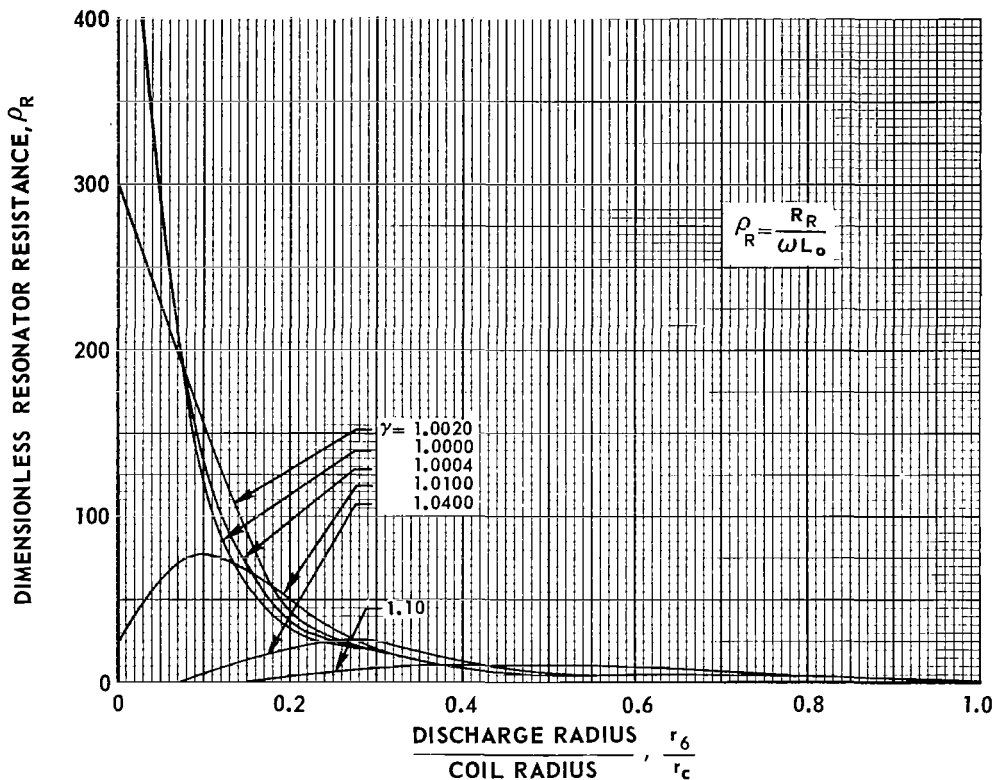a) RESONATOR RESISTANCE

b) RESONATOR REACTANCE

FIG. 20
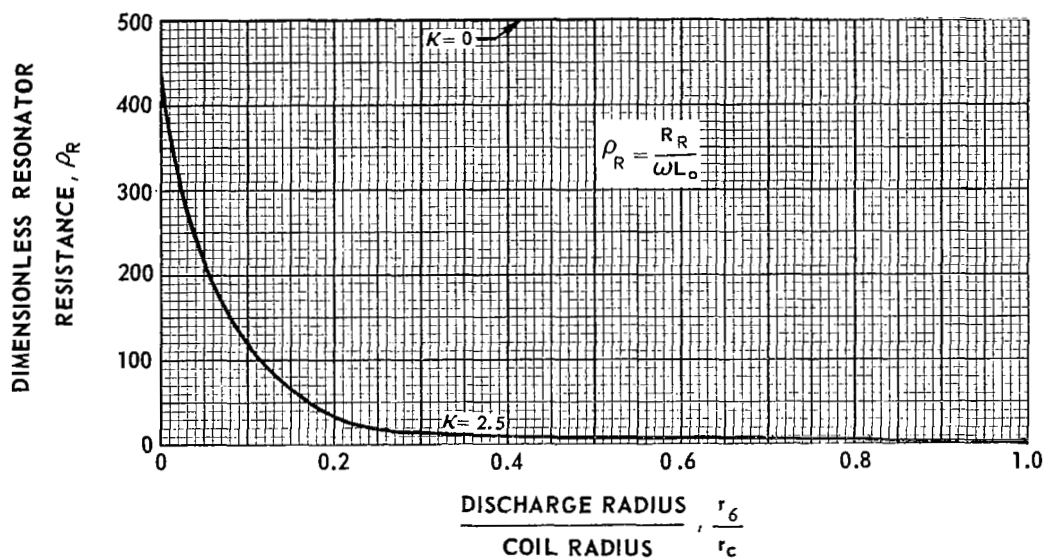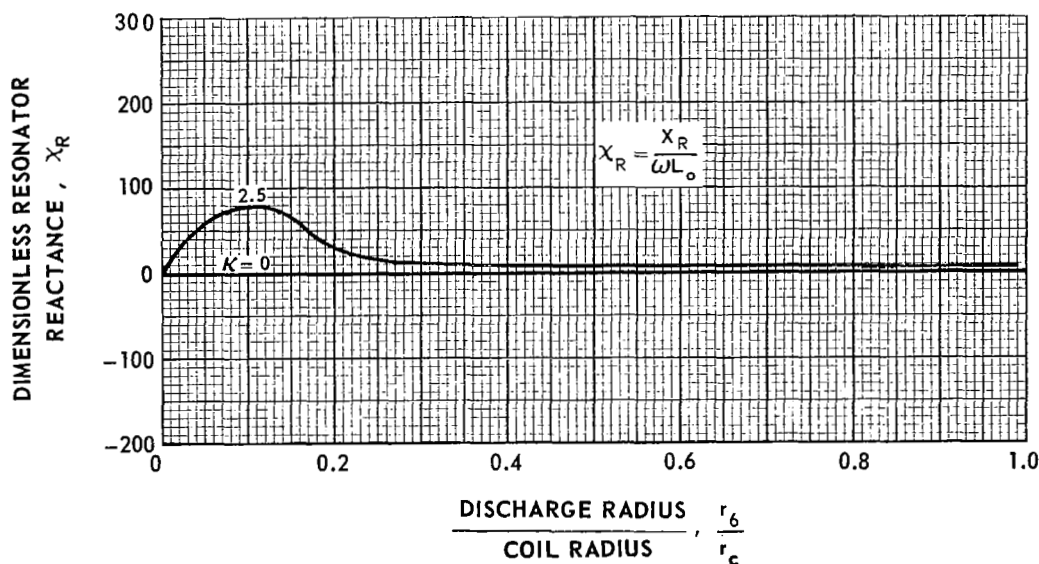
TYPICAL RESONATOR MATCHING CONDITIONS WITH DISCHARGE PRESENT
OBTAINED BY FREQUENCY SHIFT FROM UNLOADED RESONANCE

$$\kappa = \frac{1}{\sqrt{2}} \frac{d}{\delta} = 2.5, \qquad \gamma = \left(\frac{\omega}{\omega_o}\right)^2 = \left(\frac{f}{f_o}\right)^2, \qquad \frac{\omega L_o}{R_o} = 500$$

$\sigma = $ CONSTANT

a) RESONATOR RESISTANCE

$$\rho_R = \frac{R_R}{\omega L_o}$$
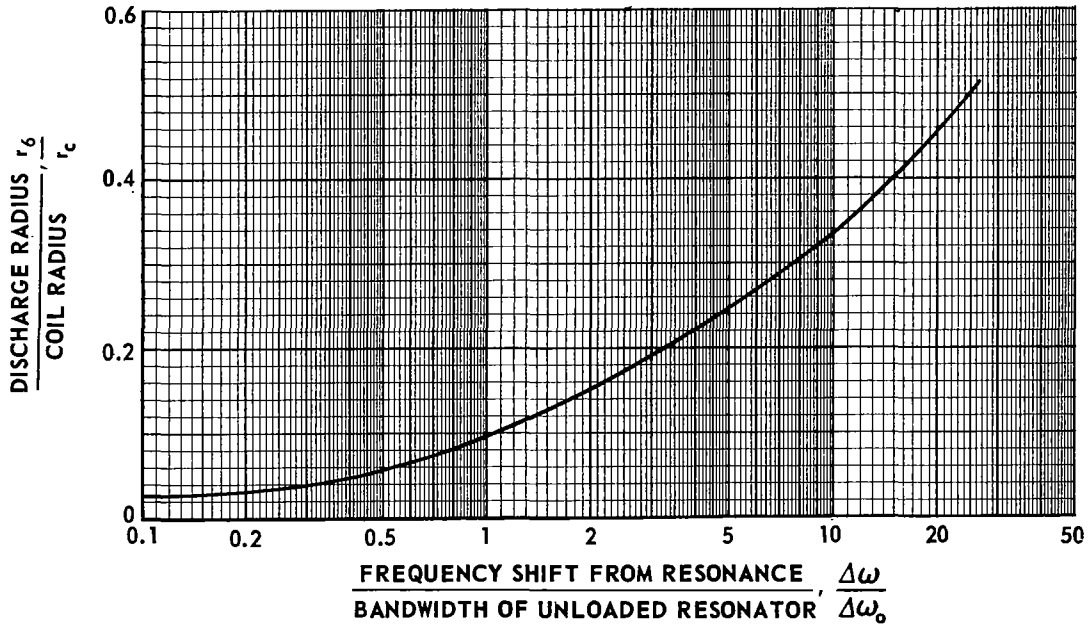
$\gamma = 1.0020$
1.0000
1.0004
1.0100
1.0400

1.10

DIMENSIONLESS RESONATOR RESISTANCE, ρ_R

DISCHARGE RADIUS , $\frac{r_6}{r_c}$
COIL RADIUS

b) RESONATOR REACTANCE

$$\chi_R = \frac{X_R}{\omega L_o}$$

$\gamma = 1.0000$
1.0004
1.002
1.01
1.04
1.10

MATCHING POINTS

DIMENSIONLESS RESONATOR REACTANCE, χ_R

DISCHARGE RADIUS, $\frac{r_6}{r_c}$
COIL RADIUS

71

FIG. 21

EFFECT OF FREQUENCY SHIFT FROM THAT OF UNLOADED RESONANCE ON DISCHARGE SIZE AND RESONATOR RESISTANCE FOR THE MATCH CONDITION THAT RESONATOR REACTANCE BE ZERO
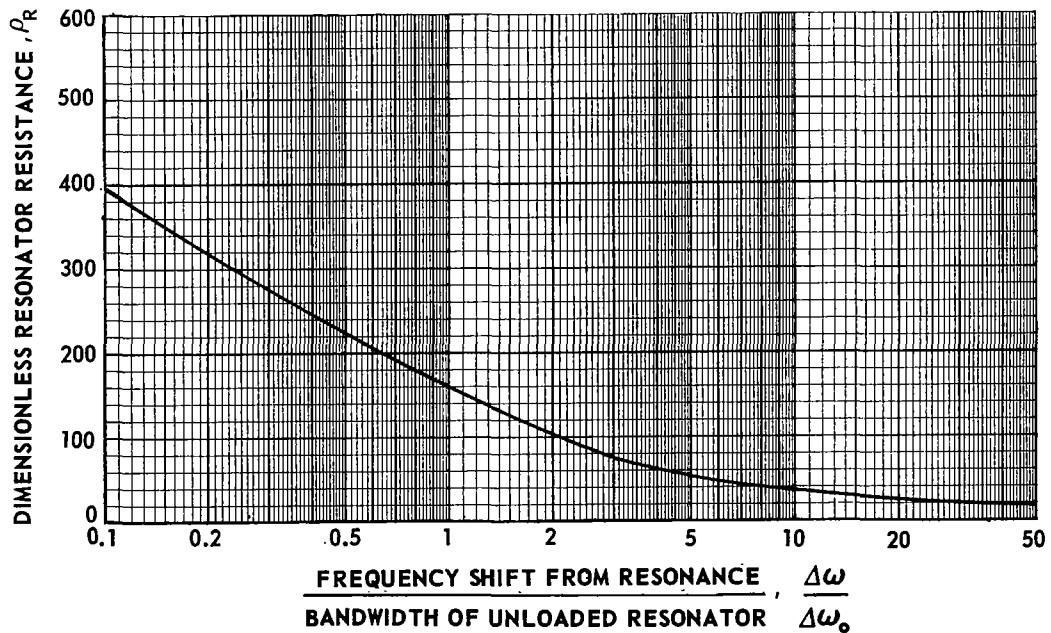
$$\Delta \omega_o = R_o / L_o, \quad K = \frac{1}{\sqrt{2}} \frac{d}{\delta} = 2.5, \quad \frac{\omega_o L_o}{R_o} = 500$$

CURVES OBTAINED BY CROSSPLOT OF DATA ON FIG. 20 FOR $X_R = 0$

a) EFFECT OF FREQUENCY SHIFT ON DISCHARGE SIZE FOR $X_R = 0$

FREQUENCY SHIFT FROM RESONANCE / BANDWIDTH OF UNLOADED RESONATOR, $\frac{\Delta \omega}{\Delta \omega_o}$

b) EFFECT OF FREQUENCY SHIFT ON RESONATOR RESISTANCE FOR $X_R = 0$

FREQUENCY SHIFT FROM RESONANCE / BANDWIDTH OF UNLOADED RESONATOR, $\frac{\Delta \omega}{\Delta \omega_o}$

72

FIG. 22

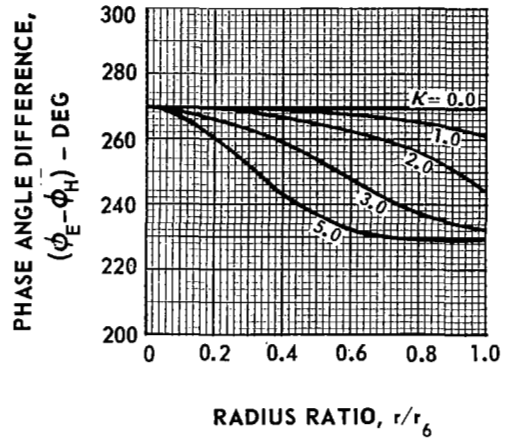# TYPICAL RADIAL VARIATIONS OF INDUCED CURRENT AND FIELD PHASE ANGLES IN AN INDUCTION HEATED PLASMA

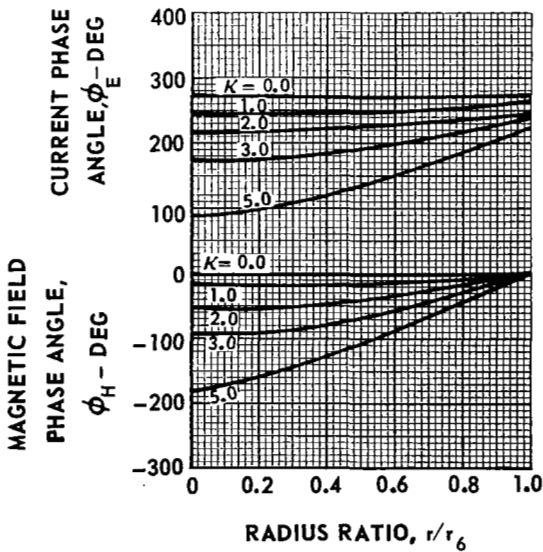$$K = \frac{1}{\sqrt{2}} \frac{d}{\delta}$$

$\sigma = $ CONSTANT

a) MAGNITUDE OF INDUCED CURRENT
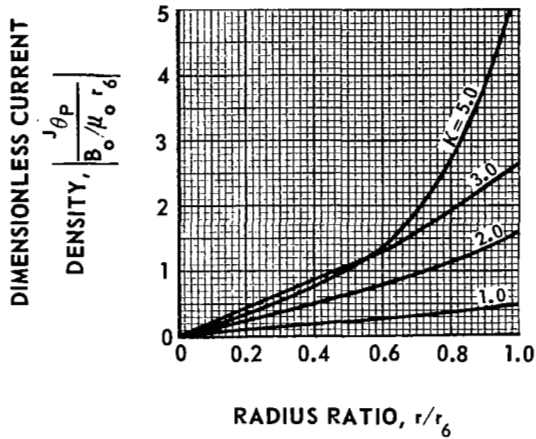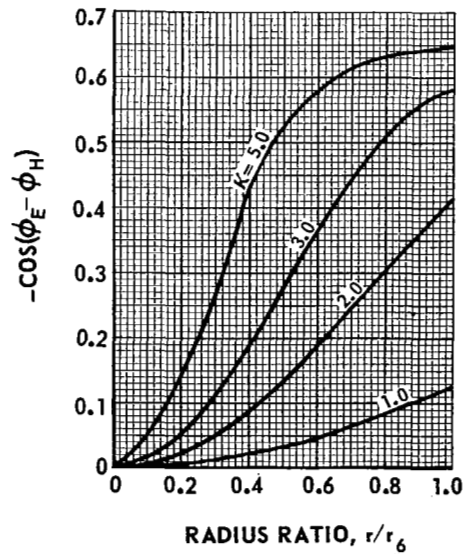
b) PHASE ANGLE DIFFERENCE BETWEEN CURRENT AND MAGNETIC FIELD
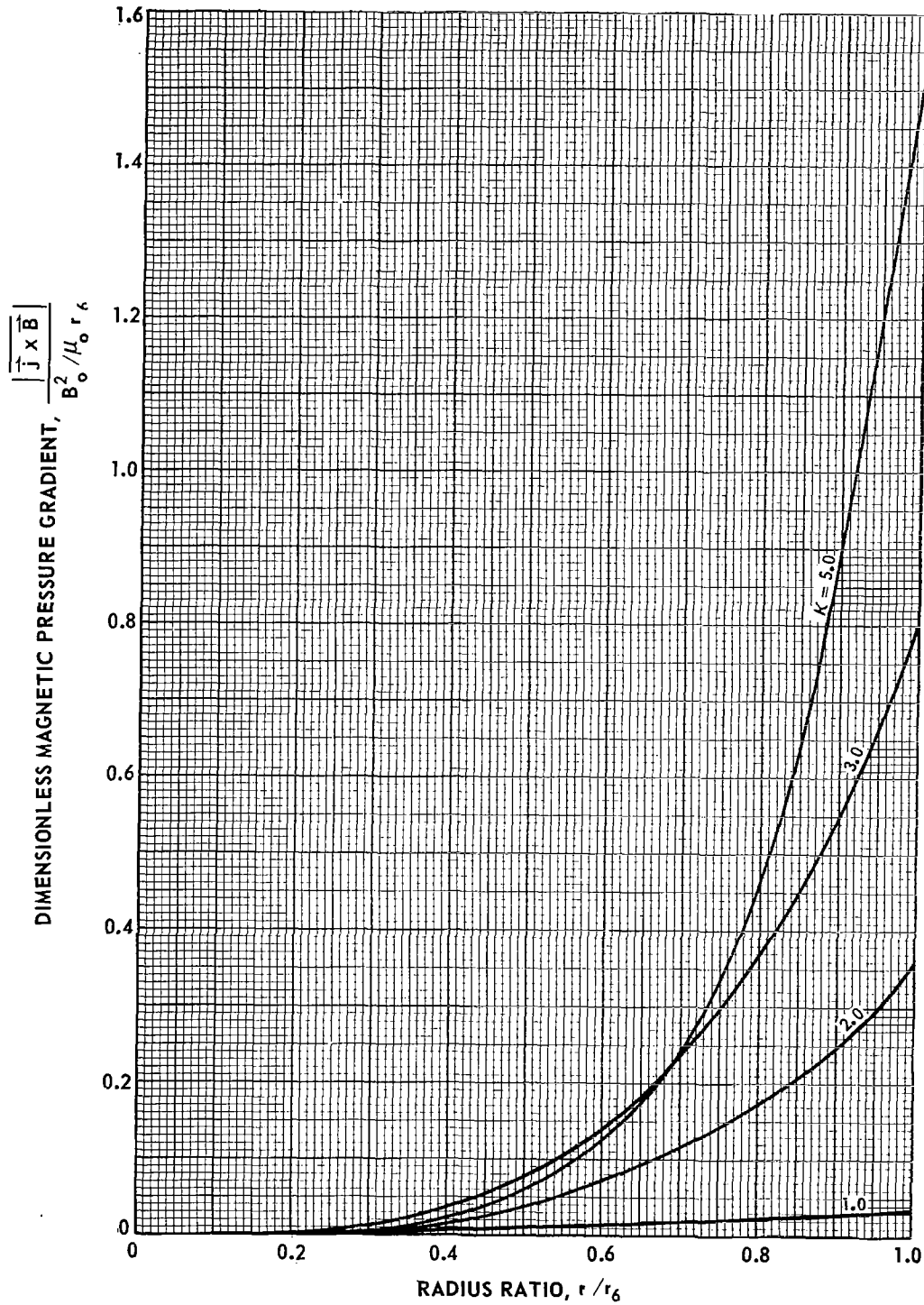
c) PHASE OF INDUCED CURRENT AND MAGNETIC FIELD

d) COSINE OF PHASE ANGLE DIFFERENCE

FIG. 23

EFFECT OF COUPLING PARAMETER ON MAGNETIC PRESSURE GRADIENT IN AN INDUCTION HEATED PLASMA

$$\kappa = \frac{1}{\sqrt{2}} \frac{d}{\delta}$$

$$\sigma = CONSTANT$$

FIG. 24

EFFECT OF COUPLING PARAMETER ON MAGNETIC PRESSURE AT THE CENTER OF AN INDUCTION HEATED PLASMA

$$K = \frac{1}{\sqrt{2}} \frac{d}{\delta}$$

$\sigma = \text{CONSTANT}$

$P_m = P_{CI} - P_{r_6}$